

FULL PAPER

Open Access



Aftershock study of the 2019 Ambon earthquake using moment tensor inversion: identification of fault reactivation in northern Banda, Indonesia

Aria W. Baskara¹, David P. Sahara^{2*}, Andri D. Nugraha², Andi Azhar Rusdin³, Z. Zulfakriza², Sri Widiyantoro^{2,4}, Wahyu Triyoso², Awali Priyono², Nanang T. Puspito², Hasbi Ash Shiddiqi⁵, Dian Kusumawati¹, Alfend Rudyawan⁶ and Erfin Elly⁷

Abstract

On September 26, 2019, an Mw 6.5 earthquake occurred 23 km northeast of Ambon City, Indonesia, followed by numerous aftershock series related to a complex fault network reactivation in the Ambon and Seram region. Using moment tensor inversion, we identify the kinematics of fault reactivation based on the focal mechanism solution of 20 aftershocks with Mw > 3.2 and analyze the earthquake sequence from both focal mechanism solutions and spatiotemporal seismicity. The MTs solution of aftershocks revealed three different characteristics of fault reactivation: (i) a 35 km long N-S oriented main fault characterized by dextral strike-slip (ii) a NE-SW reverse fault segment with a ~55° northeastward dip located in southwest Seram, and (iii) two strike-slip segments (NNW-SSE and NNE-SSW trends) and an E-W normal fault in Ambon Island. Analysis of spatiotemporal seismicity with the MTs solution suggests that the Mw 6.5 Ambon aftershock sequences can be described as follows: (i) an Mw 6.5 mainshock rupture that was primarily made up of a major strike-slip component and an insignificant minor normal fault; (ii) first aftershock cluster propagate along the main N-S ruptures, followed by the strike-slip and normal cluster in Ambon Island (iii) The reverse fault events cluster appeared next in Southwest Seram. The presence of complex strike-slip segments in Ambon agrees with the regional structure trends in Halmahera, located in the north of the study area, while the E-W oriented normal fault might be related to the eastward velocity increase in Banda Arc, which causes extensional deformation. Given that the fault reactivation identified in Ambon and Seram is located close to the densely populated urban regions of Ambon City and Kairatu, the analysis of future seismic hazards related to this fault reactivation should consider the risks in a region with complex fault settings.

Keywords 2019 Ambon earthquake, Aftershock sequences, Source mechanism, Moment tensor inversion, Fault reactivation

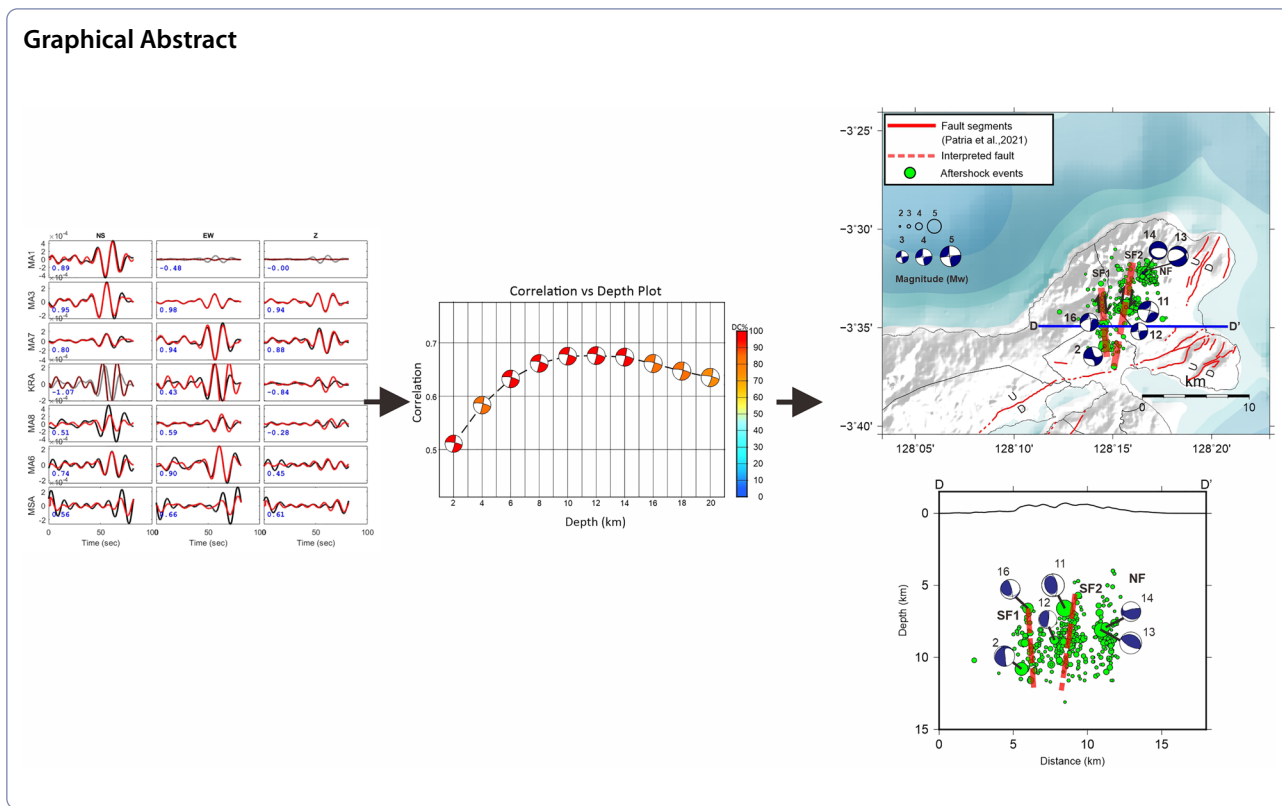
*Correspondence:

David P. Sahara
david_sahara@itb.ac.id

Full list of author information is available at the end of the article



© The Author(s) 2023. **Open Access** This article is licensed under a Creative Commons Attribution 4.0 International License, which permits use, sharing, adaptation, distribution and reproduction in any medium or format, as long as you give appropriate credit to the original author(s) and the source, provide a link to the Creative Commons licence, and indicate if changes were made. The images or other third party material in this article are included in the article's Creative Commons licence, unless indicated otherwise in a credit line to the material. If material is not included in the article's Creative Commons licence and your intended use is not permitted by statutory regulation or exceeds the permitted use, you will need to obtain permission directly from the copyright holder. To view a copy of this licence, visit <http://creativecommons.org/licenses/by/4.0/>.



Introduction

Indonesia is located in a complex tectonic region with frequent occurrences of earthquakes. In eastern Indonesia (insert map in Fig. 1a), the major plates responsible for the high seismicity are the Australian plate which moves to the north-northeast relative to Eurasia, and the Pacific plate which moves to the west relative to Australia (DeMets et al. 2010). The westward movement of the Pacific plate is the primary driving force for a series of left-lateral displacements in the northern part of eastern Indonesia, including the Yapen Fault Zone (YFZ), Sorong Fault Zone (SFZ), the Kawa Shear Zone (KSZ), as well as the Matano and Palu-Koro Faults (in Sulawesi, exclude from the insert map) (Stevens et al. 2002; Bock 2003; Watkinson and Hall 2017). The Banda Arc, which curves 180° around the Banda Sea, forms a prominent geological feature in eastern Indonesia. Its collision with the Australian continental margin contributes most to seismicity in the Banda region. The arc developed by the eastward subduction rollback as ancient cold oceanic Proto-Banda Sea lithosphere which formed a pre-existing embayment in the Australian continental margin was subducted from the Miocene onwards (Spakman and Hall 2010). This old lithosphere has been almost completely subducted under the Banda Sea. The study area is located in the northern part of the outer Banda Arc, part of the

collision zone between the Australian continental margin and the Banda Arc (Audley-Charles et al. 1979). This arc, which represents the deformation front of the fold-and-thrust belt, is mostly comprised of imbricated thrust faults and is bounded by the Timor, Tanimbar, and Seram Troughs (Audley-Charles et al. 1979; Hall R et al. 2017; Baillie et al. 2020). The northern outer Banda Arc now converges with the Bird’s Head at a rate of 30–50 mm/year in an ENE direction, oblique to the Seram Trough (Bock et al. 2003). Convergence in the Seram region is accompanied by strong seismicity dominated by shallow thrusts and strike-slip faults (Mccaffrey 1989; Engdahl et al. 1998).

Several major destructive earthquakes occurred in the northern Banda Arc (black stars in Fig. 1a), such as the 1674 and 1708 earthquakes which triggered a tsunami in Ambon, Haruku, Buru, and the surrounding regions (Harris and Major 2016); an Mw 7.8 earthquake in 1899 that struck Tehoru, Seram (Brune et al. 2010); an Mw 7.6 on 8 October 1950 close to the south coast of Ambon (Bâth and Duda 1979); and an Mw 8.2 earthquake in 1965 located in northern Buru (Løvholt et al. 2012; Patria et al. 2021). Ambon City, located on Ambon Island, is the capital of the Maluku province with a population of more than 368,987 inhabitants in 2021 (BPS: Statistics Indonesia 2021). Although this region is tectonically active and

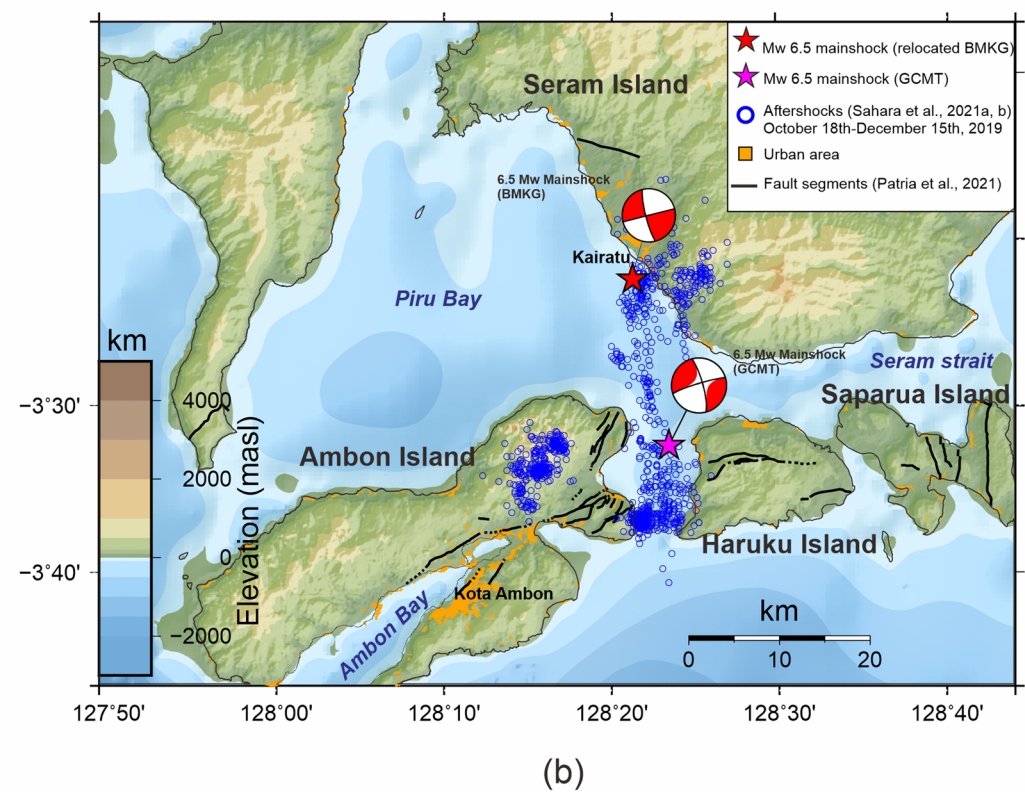
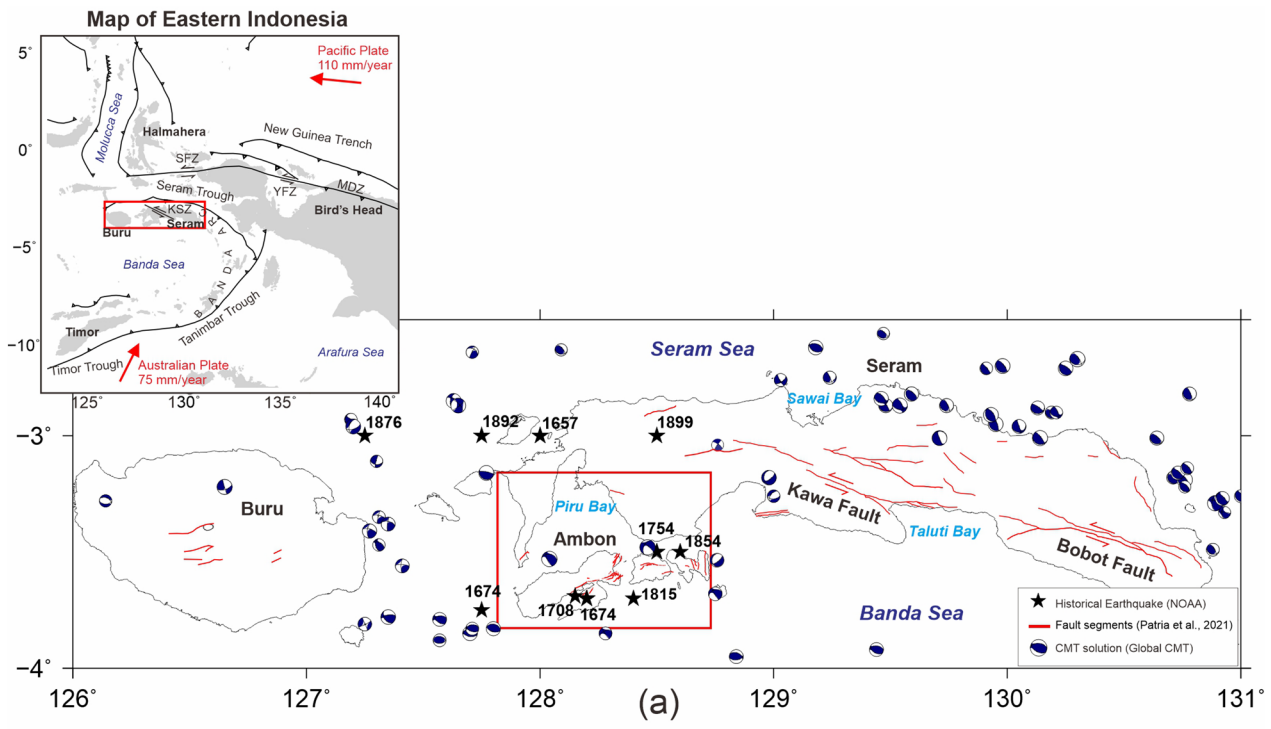


Fig. 1 a Active fault map of the northern Banda region adapted from Patria et al. (2021) shown by red lines. The epicenter of the historical earthquakes from NOAA (National Oceanic and Atmospheric Administration) from 1600 to before 1900 are presented as black stars. Centroid moment tensor solutions (navy beach balls) of events with depth < 20 km and a magnitude more than Mw 5 in the period of 1976–2018 are derived from Global CMT. **b** Map of the aftershock distributions (indicated by blue circles) in the study area derived from Sahara et al. (2021a, b) between October 18th to December 15th, 2019 recorded by local and BMKG regional networks. The epicenter of the mainshock is shown by a magenta star (Global CMT) and a red star (BMKG). Focal mechanism solutions from both agencies are inserted by red beach balls. Fault segments from Patria et al. (2021) are plotted in black lines. The area colored in orange represents the urban or populous region

experienced several historical destructive earthquakes, not all the source faults of the past earthquakes were fully understood due to the lack of marine geophysical surveys and insufficient seismic data. Thus, seismic hazards related to the active faults in this densely populated area should be analyzed further.

Recently, fault observations in this area have become more intensive. Patria et al. (2021) integrated their geomorphic feature studies with the existing dataset from geological structure, seismic, and geodetic observation to map the complex active faults in the northern Banda Arc, including Seram and Ambon (the identified faults are shown by red lines in Fig. 1a as well as black lines in Fig. 1b). The study observed that the fault system in Seram is generally divided into two different tectonic regimes. North Seram is mostly characterized by the activity of the Seram fold-and-thrust belt. Thus, features such as back-tilted marine terraces, fault scarps, and uplifted ridges are well observed there. The focal mechanism solution from Global CMT (navy beach balls) in this area added an understanding of the distribution of the thrust fault in this area. Meanwhile, Central, and east Seram, are dominated by left-lateral strike-slip faulting, which is identified by the presence of river offsets, decapitated rivers, shutter ridges, and linear valleys (Patria et al. 2021).

The ~137 km-long Kawa Shear Zone (Pownall et al. 2013), or Kawa Fault (Patria et al. 2021), with observed offsets of about ~2 km is the main significant structure in Central Seram, separated from the Bobot Fault in the east by Teluti Bay. A left-lateral strike-slip fault is also recorded in the offshore area east of Seram (Teas 2009; Patria and Hall 2017). Watkinson and Hall (2017) suggested this offshore strike-slip fault, the Bobot Fault and the Kawa Fault are part of a KSZ. Patria et al. (2021) also identified several dip-slip faults with the east to northeast strike direction in Amahai, Ambon, and surrounding islands that cut marine terraces. The Ambon Fault extends from Ambon Bay for about 34 km to the northeast coast of Ambon. Patria et al. (2021) suggested that the Ambon Fault is relatively young since it deforms the lower marine terrace surfaces of the early to middle Pleistocene age.

The most recent significant earthquake with an Mw 6.5 struck the northern Banda region on September 26, 2019, with a hypocenter located 23 km northeast of Ambon City. Sahara et al. (2021a; b) have produced an accurate seismic catalog of the aftershock events due to the seismic monitoring for 59 days using 11 local seismic networks and four regional seismic networks from Agency of Meteorology, Climatology, and Geophysics of Indonesia (BMKG). Figure 1b shows the location of the mainshock and aftershock distribution. Based on the analysis of

aftershock distribution and finite fault modeling, Sahara et al. (2021a) suggested that the Mw 6.5 Ambon earthquake occurred on an N-S-oriented fault plane 35 km in length that extends from Kairatu down to the Haruku strait, in which both south (label I in Fig. 2a) and north (label II in Fig. 2a) ends have more frequent aftershocks. In addition, there was seismicity trending NE-SW in Seram Island (label III in Fig. 2a), and seismicity trending NE-SW in Ambon Island (label IV in Fig. 2a). The widespread aftershock distribution separates into several distinct clusters raising the issue of possible reactivation of preexisting faults in this region. Interestingly, most of the aftershock sequences occurred on faults that are still unmapped. The series of mainshocks and aftershocks severely impacted the surrounding region including central Maluku and West Seram (BNPB: National Agency for Disaster Management 2019; BPS: Statistics Indonesia 2021). This data (which provides statistics about damage to houses) support that the aftershock distribution agrees well with these two most impacted regions.

Although the aftershock trends had been resolved well, there is not enough active fault data to be associated with this region's mainshock and aftershock sequences. Previous structure geological studies have shown that northeast-trending dip-slip fault scarps face southeast or northwest and cut marine terraces on Ambon and in the surrounding region and it seems too far from the seismicity clusters (see Fig. 1b) (Patria et al. 2021; Watkinson and Hall 2017). However, Ambon and Seram are in a tropical zone between latitudes 3 and 4°S, with heavy rainfall and high daily temperatures in which surficial processes may rapidly erode indications of active deformation. As a result, Ambon and Seram might have a more complex geological structure than one could map. Thus, revealing and interpreting the hidden faults is essential for assessing the potential zone of future seismic hazard. Additional information from source mechanism inversion can provide important insights to reveal the unmapped fault (in this case: fault reactivation) which could not be resolved by geological observation.

Using the aftershock sequences of the 2019 Mw 6.5 Ambon earthquake recorded by well-distributed temporary local and regional BMKG seismic networks, we attempt to identify the kinematic of possible fault reactivation. We estimated the focal mechanism of significant aftershock events by implementing moment tensor (MT) inversion using ISOLA, the ISOLated asperities software package (Sokos and Zahradnik 2008, 2013). This program is widely used in retrieving focal mechanism solutions, including when dealing with low- to moderate-magnitude earthquakes (e.g., Abdel-aal and Yagi 2017; Ataei and Rezapour 2016; Paul et al. 2018; Serpetsidaki et al. 2010). The distribution of aftershock sequences is used

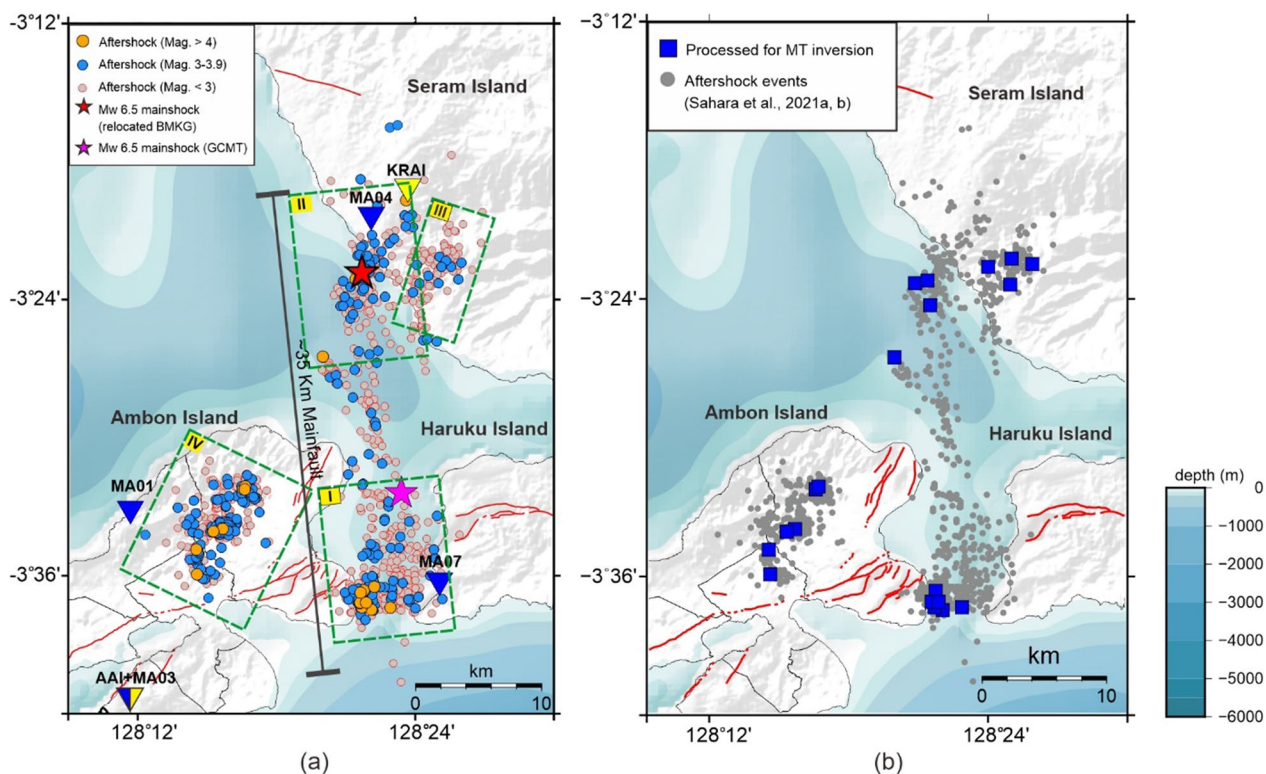


Fig. 2 **a** Hypocenters of aftershock events based on a catalog produced by Sahara et al. (2021a; b) are plotted as orange circles (magnitude ≥ 4.0), blue circles (magnitude between 3.0 and 4.0), and grey circles (magnitude < 3). The area of investigation is divided into four regions denoted by green dashed rectangles. The corresponding labels in each rectangle represent the cluster number. The epicenter of the mainshock from BMKG (red star) and GCMT (magenta star) is also inserted. Fault segments from Patria et al. (2021) are plotted in red lines. **b** Final selected events for the MT inversion process, depicted by the blue rectangles

to identify the geometry of the fault plane and a study of the focal mechanism of an individual seismic event provides kinematic information on the fault movement (e.g., Hallo et al. 2019, 2017; Herman et al. 2017; Umino et al. 2003; Zheng et al. 2010). We analyzed the major and minor MT decomposition from the mainshock’s existing MT solution to observe the possible complexity of the source mechanism and examine the possible relationship between the mainshock and the aftershock.

Data

The aftershock monitoring was conducted using a total of 15 stations, consisting of 11 three components temporary broadband stations and 4 regional BMKG stations. The distribution of the seismic networks is shown in Fig. 3. The aftershock monitoring was conducted from October 18th, 2019, 21 days after the mainshock, to December 15th, 2019. As a result of the seismic monitoring, Sahara et al. (2021a; b) produced a highly accurate catalog consisting of 1152 double-difference relocated event locations. Figure 2a shows the distribution of the relocated events and the event grouping selection for the moment

tensor processing. Here, we divided our investigation into four regions (denoted by the green dashed rectangles). The corresponding labels in each rectangle represent the region number. Regions I and II are located on the south and north of the N-S trending fault which is previously defined as the main rupture by Sahara et al. (2021a). Region III represents a separate cluster in the southwest area of Seram Island with a NE-SW orientation. Meanwhile, Region IV represents aftershocks located on Ambon Island which follow a NE-SW orientation.

We initially selected aftershock events with an Mw magnitude greater than 4.0 in the catalog of Sahara et al. (2021b). In the case of high magnitude, the moment tensor results are stable over various frequency bands ranging. When implemented in a lower magnitude, using high frequency would result in a reduction of solution quality, particularly when using a simple 1-D velocity model (Cesca et al. 2006; Petersen et al. 2021). However, we could not find enough significant events with $M_w > 4$ in regions II and III. Therefore, in these two regions, we included the events with a magnitude of $M_w 3.2-3.8$ which have a high

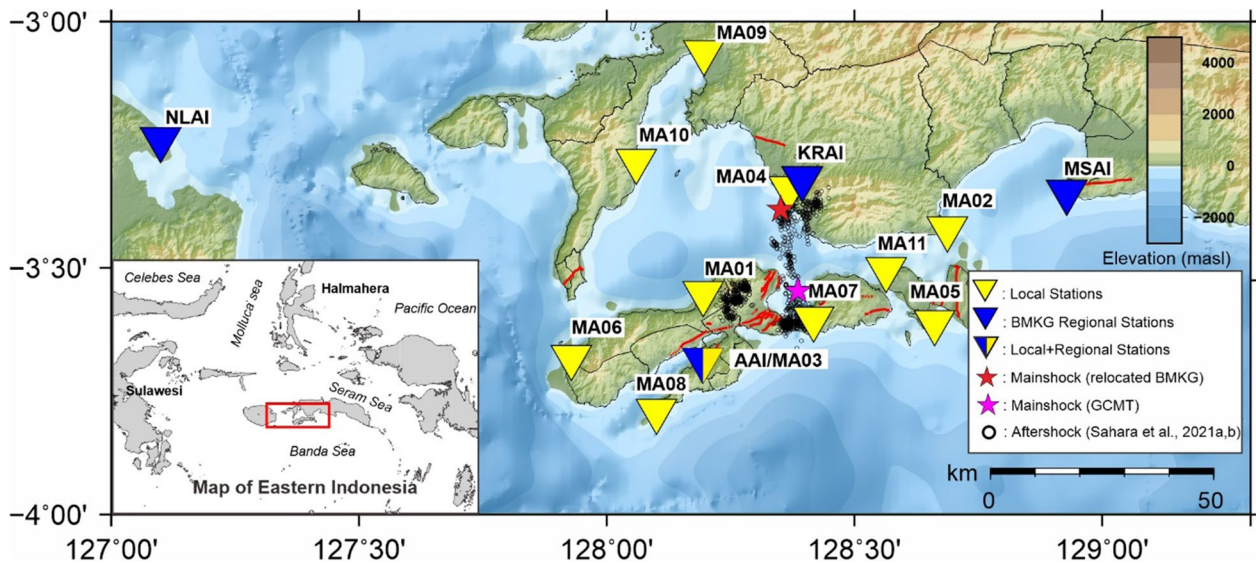


Fig. 3 Distribution of seismic stations in the study area. The reverse yellow triangles indicate the ITB local stations, the reverse blue triangles indicate the BMKG regional stations, while the reverse yellow-blue one shows the local–regional stations located close to each other. The aftershock epicenters from Sahara et al. (2021a; b) are plotted as black circles, while the magenta and red star represent the mainshock from GCMT and BMKG (relocated), respectively

signal-to-noise ratio (SNR) and were recorded by at least 5 stations. Based on these criteria, 20 aftershocks were selected for moment tensor inversion in all four

regions. Figure 2b shows the location of the selected events, while detailed information about these events is presented in Table 1.

Table 1 List of processed earthquakes from the Ambon aftershock sequence

Event ID	Origin time/GMT		Hypocenter			Error Loc. (km)			Mag. (Mw)
	YY/MM/DD	hh:mm:ss	Lat (°)	Lon (°)	Depth (km)	X	Y	Z	
1	2019/10/18	11:36:23	-3.623	128.382	8.1	0.81	1.84	5.25	4.4
2	2019/10/18	19:44:24	-3.599	128.243	10.8	1.73	0.73	1.91	4.7
3	2019/10/25	02:08:18	-3.625	128.368	9.0	0.49	0.96	1.55	4.5
4	2019/10/26	05:04:22	-3.375	128.401	10.0	1.23	2.33	2.77	3.2
5	2019/10/26	19:02:58	-3.611	128.363	9.3	0.50	0.80	1.83	4.2
6	2019/10/30	05:04:52	-3.388	128.417	7.7	1.08	2.55	4.05	3.3
7	2019/11/8	04:37:07	-3.403	128.359	3.5	1.20	0.78	2.97	3.8
8	2019/11/9	03:29:20	-3.623	128.362	8.3	1.38	1.77	2.19	4.3
9	2019/11/9	15:39:46	-3.619	128.360	8.0	0.56	0.96	2.11	4.1
10	2019/11/11	04:35:25	-3.387	128.348	6.1	0.80	0.88	3.02	3.5
11	2019/11/12	10:10:40	-3.566	128.261	6.6	0.73	0.95	2.98	5.1
12	2019/11/12	11:01:44	-3.568	128.255	8.8	0.53	0.69	1.84	4.1
13	2019/11/15	21:02:01	-3.537	128.276	8.1	0.70	0.47	3.26	4.9
14	2019/11/15	22:30:10	-3.535	128.278	7.9	0.59	0.91	2.70	4.2
15	2019/11/17	05:11:21	-3.373	128.433	7.0	0.80	1.03	2.11	3.7
16	2019/11/18	09:04:29	-3.581	128.242	6.6	0.67	0.78	2.22	4.4
17	2019/11/18	13:11:19	-3.369	128.418	9.3	1.10	1.53	3.09	3.3
18	2019/11/20	21:43:27	-3.619	128.365	8.2	0.51	0.94	1.84	4.1
19	2019/12/4	13:48:07	-3.441	128.333	9.8	1.07	0.72	2.98	4.3
20	2019/12/14	19:43:11	-3.385	128.357	12.2	0.87	4.48	3.85	4.1

Methods

Moment tensor inversion

The moment tensor inversion is implemented to the aftershock data using the ISOLA code developed by (Sokos and Zahradník 2008, 2013). In this approach, the source is assumed to be made up of a sequence of point sources of various focal mechanism. They proposed that the moment tensor at a given position and time centroid can be considered a linear combination of the six components of the moment tensor (MTs). Calculations of MTs are performed by minimizing the difference between the observed and synthetic displacements. The match between the observed and synthetic data is characterized by variance reduction (VR), i.e., greater VR indicates better inversion matching and vice versa. In our case, we inverted the deviatoric moment tensor, in which we were more concerned about the best-fitting DC source. In terms of the fault-related case, we expect the result to be a shear faulting with significant DC.

As a preprocessing procedure, we initially selected the waveform based on SNR by visually inspecting in all components for each station per event. We set the time window at 80–100 s length and then the instrument response was deconvolved to obtain displacement seismograms that were bandpass filtered between 0.04 and 0.12 Hz. This range is the minimum and maximum frequency bands utilized in the MT inversion to reduce the influence of low and high-frequency noise. Considering the range of aftershock depth based on the catalog (Sahara et al. 2021b), the trial source was calculated at various points below the epicenter from 2 to 20 km with an interval of 2 km. At each source depth, Green's function calculation is performed using the frequency wavenumber method (Bouchon 1981). This step was carried out to test the correlation between the observed waveform and the synthetic waveform of both vertical and horizontal components. For each source depth, the source time shift is also defined to form a 2-D correlation contour (see Fig. 6b). The inversion process is carried out at each depth and time shift where the optimal solution with the highest correlation will be determined as the best fit through an analytic grid search. We manually inspected and selected well-correlated waveforms and removed the poor ones in each iteration of the MT inversion. In the end, around 5 to 7 stations were used for the final MT inversion for each event.

Accounting for the quality parameter and uncertainty of the MT

We used VR as the main evaluation of the inverted moment tensor quality as it represents how good the fitting between the real waveform and the synthetic

waveform. In addition, we also used Focal Mechanism Variability Index (FMVAR), Condition Number (CN), Space–Time variability index (STVAR), and DC percentage to assess the reliability and robustness of the MT solution. CN represents the quality related to the station-event configuration, STVAR and FMVAR are related to the robustness of the solution in the space–time dimension, while DC measures the percentage of the shear slip on a planar fault (detailed explanations of the quality parameters, including the calculation and visualization, are served in the additional files). We took events that satisfy at least four out of five criteria based on Sokos and Zahradník (2013) as follows: (i) $VR > 50\%$, (ii) $CN < 10$, (iii) $FMVAR < 30^\circ$, (iv) $STVAR < 0.3$, (v) $DC > 70\%$.

We also assessed the MTs solution uncertainties for all events to add the control quality factors. In this study, we only calculated relative uncertainty assessments, in which we investigated the resolvability of the DC component of moment tensor solution without using actual waveforms (Sokos and Zahradník 2013). In this case, errors of the model parameters are related to data errors through Green's functions matrix, G . As a result, we may analytically examine a given source-station configuration, quantify the uncertainty of a certain focal mechanism, and prescribe the data variance σ_d^2 and missfit $\Delta\chi^2$ (Zahradník and Custódio 2012). The uncertainty of MT solutions was calculated by averaging the 5D error ellipsoids (for deviatoric MT) on each position and source time. The ellipsoids are constructed numerically by regularly sampling the parameter space around the assumed moment tensor, in which the shape and orientation are determined by the source-station configuration, frequency ranges, and the crustal model used. From the error ellipsoid, a statistical set of the strike, dip, and rake is obtained whose histograms can be constructed (the detailed procedure and example of the uncertainty calculation is presented in the additional file).

Major and minor moment tensor decomposition

Unlike the MT analysis on the aftershock data, in which we just used deviatoric MT in the processing, for the mainshock, we would further carry out a deviatoric MT decomposition into major and minor DC MTs (Kanamori and Given 1982). Both decomposed MTs may be physically interpreted by the complex geometry of the rupture. However, Jost and Herrmann (1989) pointed out that these typical decompositions may be suitable in some specific cases. This means that the physical interpretation of the major and minor DC MTs should be confirmed by other data derived from the rupture (e.g., local tectonic settings, source mechanisms of other events, or slip inversion on a segmented fault) (Hallo et al. 2017, 2019). In the case of 2019 Ambon earthquake, the coseismic slip

model from Meilano et al. (2021) has clarified and supported the interpretation of the rupture. As additional support from the perspective of MT analysis, we would like to conduct this MT decomposition to examine the possible complex rupture. Furthermore, comparing these decomposition results with the distribution of MT solution of aftershock could give an understanding of the relationship between the mainshock and the aftershock.

The major DC MT is the best approximation of a non-shear (non-DC) MT by a shear (DC) source. As in (Wallace 1985), assume absolute values of deviatoric MT eigenvalues $|\lambda_1| \geq |\lambda_2| \geq |\lambda_3|$ with respective eigenvector v_1, v_2 , and v_3 , the major and minor DC MTs with preserved dominant axis can be formulated as follows:

$$M_{major} = \lambda_2(-v_1^T v_1 + v_2^T v_2) \quad (1)$$

$$M_{minor} = \lambda_3(-v_1^T v_1 + v_3^T v_3) \quad (2)$$

The deviatoric condition $\lambda_1 + \lambda_2 + \lambda_3 = 0$ applies. The dominant eigenvector v_1 refers to the direction of either P- or T-axis, based on the sign of the dominant eigenvalue λ_1 (Hallo M et al. 2017). The python code from Hallo et al. (2017, 2019) is used to perform major and minor MT decomposition.

As the MTs solution of the mainshock, due to the limited local network provided (beyond our local monitoring), we considered the existing data from both Global CMT (Ekström et al. 2012) and GFZ Potsdam (Saul et al. 2011). For both two MTs solutions, we take advantage of the Full MT concept and decompose it into major and minor DC MTs assuming preserved P-axis (Wallace 1985; Hallo et al. 2017, 2019). The more reliable result was analyzed further by considering the aftershock's MT solution.

1D crustal model

We tested several crustal models to select the most suitable one for representing the study area's subsurface structure which is reliable for Green Function calculation. The four models were selected, namely the PREM (Preliminary Reference Earth Model) (Dziewonski and Anderson 1981), a crustal model for the central part of Java (Koulakov et al. 2007), a crustal model for eastern Indonesia (Sabtaji and Nugraha 2015), and a new regional crustal model around Ambon derived from Sahara et al. (2021a). The regional model from Sahara et al. (2021a) is an updated 1D velocity model utilized by implementing VELEST program (Kissling et al. 1995) which used AK135 as initial crustal model to better fit the simple geological model in the Ambon region. Figure 4 describes the value of P and S wave velocity and the layer depth of all models.

The Green Function is calculated using four crustal models, followed by an MT inversion. We performed MT inversion tests for the Mw 5.1 aftershock event that occurred on November 12th, 2019 at 10:10:40 UTC. Figure 5 depicts the MT results in the form of correlation graphs using four distinct crustal models. For each model, the graphic shows the focal mechanism solution derived from ten trial source numbers, and the correlation values between observed and synthetic waveforms. The centroid moment tensor (CMT) solution from Global CMT (navy beach ball) is also present for a more accurate comparison. The results indicate that the crustal model proposed by Sahara et al. (2021a) has the highest correlation value and provides a more stable solution which is relevant to the Global CMT results. Although the Sabtaji and Nugraha (2015) model has a fairly high correlation, the focal mechanism solution is not consistent if compared to the solutions presented by the crustal model from Sahara et al. (2021a). The correlation values for the PREM and Koulakov models are relatively low (below 0.5). Furthermore, the MT solutions using koulakov model have a different mechanism from the global CMT reference solutions, which could lead to misinterpretation. Finally, we used the crustal model from Sahara et al. (2021a) to calculate Green Function calculation for all events during the inversion process.

Results

MTs solution of aftershock events

An example of the inverted MTs obtained in this study is presented in Fig. 6. We plot the MTs inversion results for an aftershock event that occurred on November 12th, 2019 at 10:10:40 UTC with a magnitude of 5.1 Mw (event ID 11). It was the greatest aftershock recorded by our network. The frequency range used for this earthquake is 0.04–0.10 Hz. Figure 6a shows the correlation between the observed (black) and synthetic (red) waveforms for all the components of 7 stations. VR values for each station are indicated in blue numbers, in which the higher the absolute value, the better the correlation is. We deactivate the E-W and vertical component of MA01 (ID MA1) stations due to the poor correlation (depicted by the grey waveforms). The elimination is also applied to the N-S component of stations KRAI (ID KRA) for the same reason. The average VR value of all stations is 71.9% (see Table 2). A plot between the source time shift and trial source numbers in correlation contours is plotted in Fig. 6b. The background color shows the correlation value a scale of 0–1, while the beachball color represents the DC percentage. Here, the maximum correlation is obtained for a source time shift of ~1.5 s which corresponds to the increased size of the resultant beachball shown in red. The graph of correlation vs depth is also

1D velocity models used in the MT inversion test

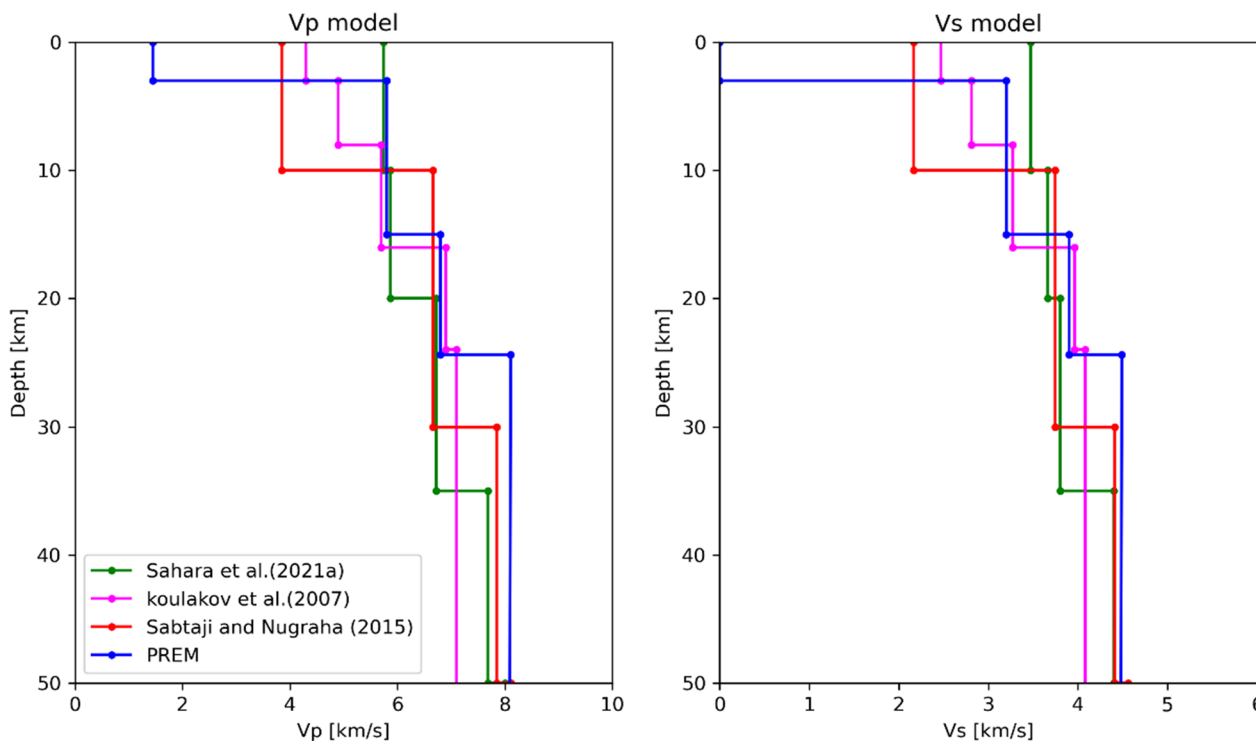


Fig. 4 Velocity models used in the MT inversion test, consist of Vp (left) and Vs values (right) in km/s for each layer depth in km. The four models consist of: (i) Sahara et al. (2021a), shown by green lines; (ii) Koulakov et al. (2007), shown by magenta lines, (iii) Sabtaji and Nugraha (2015), shown by red lines, and (iv) PREM model (Dziewonski and Anderson 1981), shown by blue lines

shown (Fig. 6c). We can see that the maximum correlation is obtained for a focal depth of 12 km with 94.5% DC of the beach balls. Figure 6d shows the map view of the event epicenter (a black star) and the stations used in the MT inversion (reverse red triangle).

Figure 7a shows the distribution of the focal mechanism solution. Our MTs inversion results suggest that strike-slip mechanisms predominated in the 2019 Ambon aftershock sequences, followed by minor normal and reverse faults. The label number in the corresponding beachball indicates the event ID as shown in Table 2. The ternary diagram adapted from Frohlich (1992) and Hallo et al. (2017, 2019) is presented in Fig. 7b to indicate the style of faulting of each MTs solution.

Table 2 shows the MT solutions of 20 events, which consist of nodal plane parameters (strike, dip, and rake), the frequency band used, magnitude, DC percentage, the four quality parameters (VR, CN, FMVAR, and STVAR), and nodal uncertainties. Table 2 shows that almost all solutions fit the criteria, except the bold and underlined values. The DC percentages are significant (in the range between 70 and 95%), with 80.9% on average. The VR is consistent in the range of 51–72% with 59.7% on average.

For STVAR values, 5 of 20 events are out of the criteria (event ID 6, 7, 10, 16, and 20), while event ID 4 and 15 does not fit the CN criteria. However, the values of both events in those two parameters still have small differences from the threshold criteria with a maximum gap of 4.9. For FMVAR, all events are in the criteria range, showing that the solution is stable around the optimum correlation value.

The uncertainty values for nodal parameters (strike, dip, and rake) for 20 events is shown in Additional file 1: Fig. A22 and Additional file 1: Table A1 in the additional files. The average value of uncertainties for the dip, strike, and rake is 8.80°, 4.64°, and 10.29°, respectively. The visualization of the nodal uncertainty (Table A2 column 8) shows that the uncertainty values are relatively small, to represent the coherence solutions of all the sampling nodal planes.

MTs solution of the mainshock and its major and minor MT decomposition

Figure 8 below shows the result of the MT decomposition from two MT solutions derived from the global CMT and GFZ. In general, both MTs solutions were decomposed

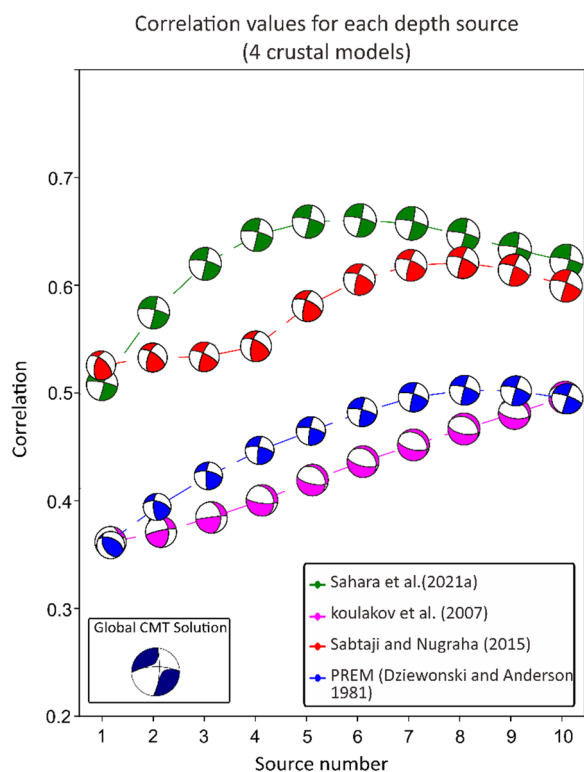


Fig. 5 MT solutions in a correlation diagram by implementing different crustal models. The graphic shows the focal mechanism solution derived from ten different trial source numbers, as well as the correlation values between observed and synthetic waveforms. The crustal model from Sahara et al. (2021a), Koulakov et al. (2007), Sabtaji and Nugraha (2015), and PREM model are, respectively, shown by green, magenta, red, and blue beach ball solutions. The MT solution from Global CMT (navy beach ball) is also inserted as a reliable comparison

into major strike-slip and minor normal fault. For the global CMT solution, the non-DC MT is decomposed into a combination of strike-slip and the normal fault with 84% and 16% scalar seismic moment ratios, respectively. Meanwhile, the solution from GFZ which has a large non-DC component is decomposed into a combination of strike-slip and the normal fault with 68.1% and 31.9%, respectively.

Discussion

We observed heterogeneity of MT solutions corresponding to different clusters. The strike-slip events were primarily associated with Regions I and II (the main N-S rupture), as well as a portion of Ambon Island (Region IV), while events with normal fault mechanisms were observed in the northern part of Ambon Island. Interestingly, we also identified a NE-SW reverse fault in Region III, southwest of Seram, where the aftershock’s trends and dip direction corresponded with the focal mechanism

solutions. We discuss the mechanism of events in each region. In addition, we also analyze the MTs decomposition result of the mainshock, and spatiotemporal seismicity of the aftershock sequences.

Analysis of region I and II (MTs solution along the main N-S rupture)

The Mw 6.5 2019 Ambon mainshock occurred on an N-S trending strike-slip fault with a rupture length of about ~35 km from Kairatu down to the Haruku strait (Sahara et al. 2021a). We identified that most of the strike-slip faults of the aftershock sequence was located along this mainshock rupture. We chose the N-S nodal plane as the fault plane in these regions since it corresponds to the rupture length as well as the aftershock trends.

Figure 9a shows the map view of focal mechanism distribution along the N-S main rupture (region I and II) with two-line sections both in the north and south including the hypocenters in a radius of 6 km (inside the blue dashed rectangles). We plotted cross-sections map to provide a better geometric illustration of the aftershocks distribution and their focal mechanism solutions (Fig. 9b, c). The red dashed lines on the figure depict the average fault dip angles inferred from both the aftershock trends and focal mechanisms. We observed that all strike-slip mechanisms in the south (Fig. 9b) have large dips angles which are mostly westward with strike orientations N-S. The average westward dip of events at the southern end of the main fault is 77.3°. In the north (Fig. 9c), four focal mechanism solutions consistently show a strike-slip mechanism with a lower dip angle compared to the south with an average of 69° eastward.

The change in dip direction along the N-S main fault from westward in the south to eastward in the north that is revealed in this study might refer to the transition zone of the possible bend fault geometry in the north, where the NE-SW oriented reverse fault (discussed in the next section) appears roughly 5 km east of the northern strike-slip. A bent fault system with different dips also occurred in the 2016 Kumamoto, Japan, earthquakes. It propagates on a near-vertical dip on one side of the bend and a northwestward dip on the other side. In this case, the inflection point represented the boundary of the two different ruptures (i.e., a rupture from the foreshock and the mainshock) and formed a ~10 km-long seismic gap (Asano and Iwata 2016; Fukahata and Hashimoto 2016; Lozos 2021). The presence of a less seismic zone of the 2019 Ambon earthquake is found in the central part of the main N-S rupture or between region I (in the south) and region II (in the north) (denoted as the red dashed

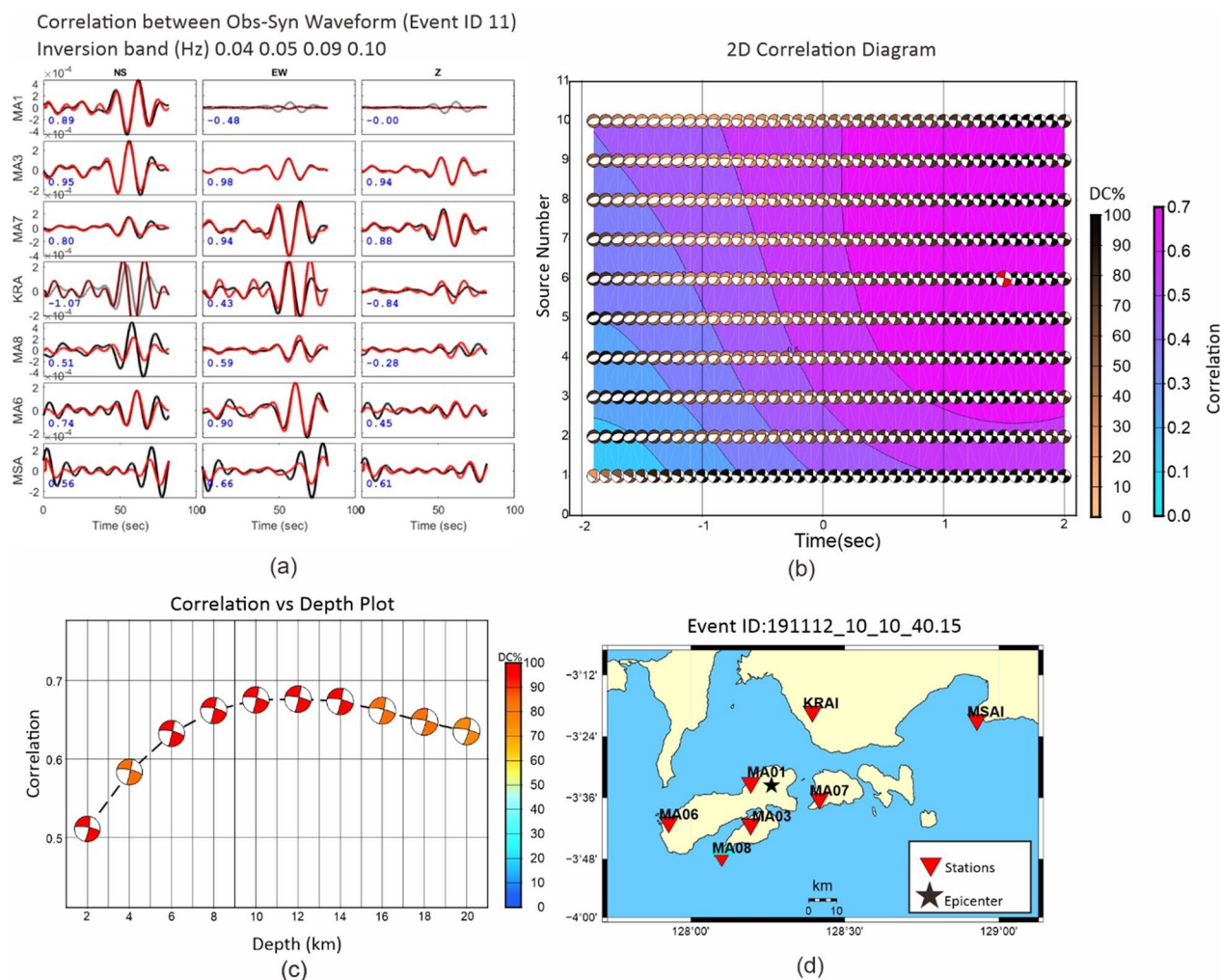


Fig. 6 Inversion results for the Mw 5.1 aftershock earthquakes (corresponding to Event ID 11 Table 2) using ISOLA. **a** The correlation between the observed (black) and synthetic (red) waveforms for all the components of all the stations are shown. VR values for each station are indicated in blue. The frequency range used for this earthquake is 0.04–0.10 Hz and is shown at the top of the figure. **b** A plot between the source time shift and trial source number in correlation contours. The color scale of the correlation values is shown on the right. The maximum correlation is obtained for a source time shift of ~1.5 s. The resultant beachball is increased in size and shown in red. **c** The plot of correlation with depth is shown. Maximum correlation is obtained for a focal depth of 12 km with 94.5% DC of the beach ball. **d** Map of stations used in the MT inversion, showed by a red reverse triangle. The event epicenter is shown as a black star

circle shadow in Fig. 9a). A further study of bathymetry structure is required to assess the variation of the main fault dip direction.

We also found that differences in dip angles in the north and south affect the direction and length of the rupture. The transition from vertical to nonvertical dip along a strike-slip fault can stop rupture from propagating through the entire fault due to the rupture deviation (Lozos 2021). This might affect the rupture propagating longer to the south direction, characterized by a high dip angle, than continuing rupture to the north, which has a shallower dip angle.

Analysis of region III (MTs solution in the southwest of Seram)

In the north, the aftershock distribution forms two distinct subclusters. Beside the north end cluster with strike-slip mechanisms (Region II), another cluster around 5 km further east shows a reverse fault mechanism striking NE-SW. This reverse fault is parallel with a surface fault mapped by Watkinson and Hall (2017) that was identified from a NE-SW lineament interpreted as an unknown fault from the Seram digital elevation model (SRTM). However, the fault is not identified in the most current geological study by Patria et al. (2021). Figure 10a

Table 2 Parameters of MTs solutions for 20 selected aftershock events with the quality parameters

Event ID	strike1/dip1/rake1 (°)	strike2/dip2/rake2 (°)	frequency band (Hz)	Magnitude (Mw)	DC (%)	VR ^a (%)	CN	STVAR	FMVAR
1	181/79/139	280/50/15	0.05–0.11	4.7	82.0	54.9	2.1	0.23	9+– 14
2	350/83/163	82/73/7	0.05–0.12	4.4	78.4	51.4	3.0	0.23	5+– 3
3	187/74/-162	92/73/-17	0.05–0.1	4.1	80.9	59.8	9.3	0.19	2+– 1
4	173/78/78	38/18/134	0.05–0.11	3.2	77.1	72.2	13.1	0.20	16+– 10
5	185/76/-158	90/69/-15	0.05–0.11	4.0	74.3	58.7	5.5	0.02	3+– 3
6	238/57/121	11/44/52	0.04–0.11	3.3	85.4	58.7	1.9	0.62	5+– 3
7	7/69/-158	269/70/-22	0.05–0.11	3.3	76.5	56.7	2.2	0.66	15+– 8
8	184/80/166	277/76/10	0.04–0.1	3.8	95.2	62.6	2.0	0.05	4+– 2
9	190/82/-180	100/90/-8	0.04–0.11	3.9	77.1	63.6	2.3	0.13	4+– 3
10	355/69/168	89/79/22	0.05–0.11	3.2	75.9	52.6	2.4	0.37	13+– 9
11	14/82/-168	283/78/-8	0.04–0.10	5.3	94.5	71.9	2.5	0.29	4+– 3
12	173/82/178	263/88/8	0.05–0.11	4.6	89.4	56.00	4.2	0.12	4+– 3
13	300/38/-40	64/67/-121	0.04–0.07	5.7	70.2	56.10	5.6	0.20	17+– 12
14	270/68/-99	113/24/-69	0.04–0.09	5.2	70.0	58.16	5.1	0.18	10+– 8
15	198/45/90	18/45/90	0.05–0.11	3.4	79.4	62.7	14.9	0.04	14+– 14
16	257/61/-16	355/76/-150	0.04–0.08	4.3	77.1	56.00	8.8	0.42	14+– 8
17	226/53/94	40/37/85	0.04–0.11	3.4	92.2	61.1	2.1	0.04	2+– 1
18	181/73/-165	87/76/-18	0.05–0.11	3.7	73.9	67.7	5.0	0.14	7+– 8
19	94/69/-13	189/78/-158	0.04–0.11	3.9	74.4	56.4	3.2	0.06	5+– 4
20	91/78/30	354/60/166	0.04–0.11	4.2	95.3	57.00	4.6	0.32	9+– 5

The bold and underlined numbers indicate that the quality parameter values are out of the criteria

^a Here, VR represents the average VR of all station's components used in the MT inversion

and b respectively shows the map view and the vertical cross-section of the focal mechanism solution with aftershock hypocenters that occurred in the northern part of the study area. The aftershock distributions and the focal mechanism solutions are well correlated, supporting the presence of the reverse fault with an average dip $\sim 55^\circ$ northwestward, indicated by the red dashed line.

The presence of a reverse fault, as well as faults with strike-slip mechanisms, might be linked to the Coulomb stress change (ΔCFS) calculated by Sahara et al. (2021a), who observed positive stress changes in the north, hypothesizing that high CFS concentrations at the northern tip of the main rupture could reactivate minor faults. Based on the Coulomb stress transfer (ΔCFF) calculation imparted by the mainshock to the existing fault, the NE-SW oriented fault in Seram also shows a stress increase value of more than 1 bar. This indicates that some of the reverse fault aligned NE-SW in Seram

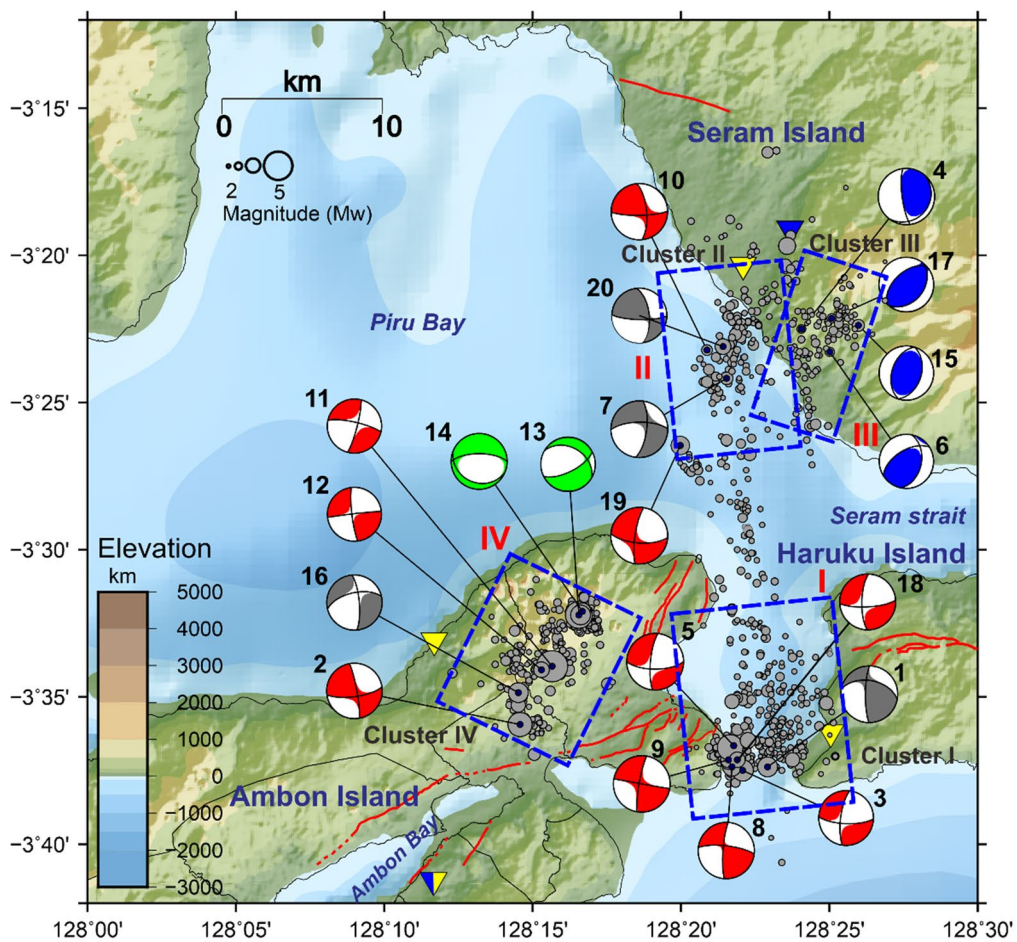
Island which experienced high-stress transfer had been reactivated.

Analysis of region IV (MTs solution in Ambon Island)

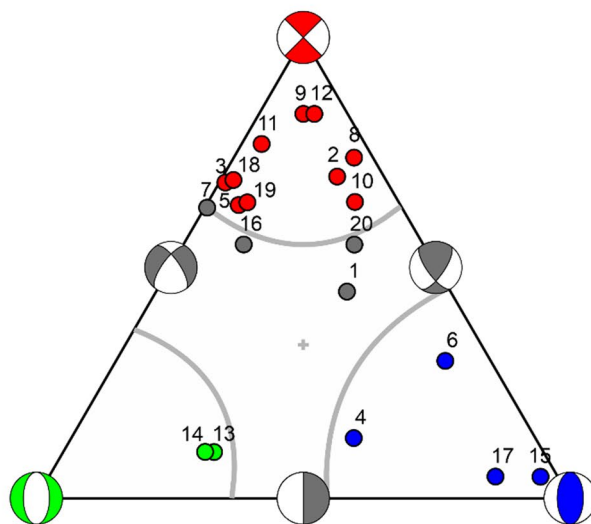
The onshore fault mapping by Patria et al. (2021) observed the presence of several active faults with dip-slip mechanisms distributed along the regions located south of the Northern Banda Arc (i.e., Amahai (Amahai fault), Saparua (Saparua Fault), Ambon (Ambon Fault), and Buru (Rana Fault) (Fig. 11a). The major trends of these faults are in E-W, N-S, and NE-SW. We also inserted the CMT solution from Global CMT which is associated with inland fault from events with depth < 20 km and a magnitude more than Mw 5 in the period of 1976–2018. The strike orientation of the normal fault solution agrees with several faults (i.e., E-W oriented Amahai Fault and N-S oriented Saparua Fault).

(See figure on next page.)

Fig. 7 a Map of the focal mechanism solutions derived in this study. The MTs solutions are plotted with colored beachballs adapted from Frohlich (1992) and Hallo et al. (2019, 2017). The number represented by black labels above the beachball corresponds to the event ID as shown in Table 2. Hypocenter locations from Sahara et al. (2021a; b) are plotted in grey circles based on magnitude size. The blue dashed rectangle shows the region of investigation. The land fault data were derived from Patria et al. (2021), depicted by red lines. **b** Distribution of all fault plane solutions of aftershock events in a ternary diagram, adapted from Frohlich (1992) and Hallo et al. (2017, 2019)



(a)



(b)

Fig. 7 (See legend on previous page.)

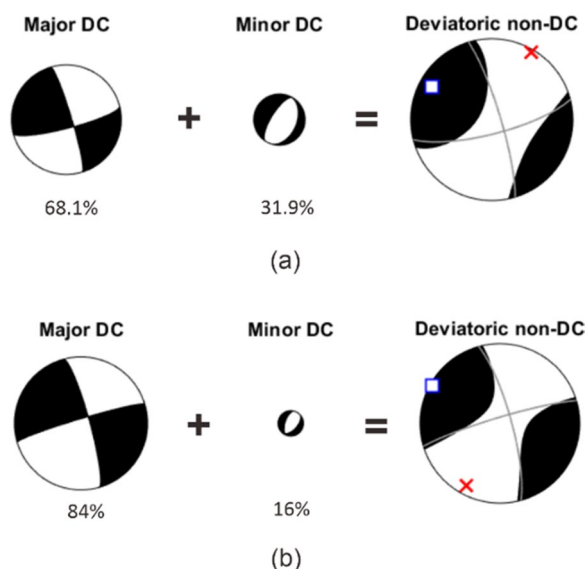


Fig. 8 Major and minor DC MT decomposition of the non-DC MT solution for the Mw 6.5 Ambon mainshock shown by the trinity of beach-ball: **a** GFZ Potsdam, **b** Global CMT solution. The size of the beach ball is proportional to their respective scalar seismic moment

In the current study, we observed three fault subclusters in Ambon Island (Fig. 11b, c): (1) the oriented NNW-SSE strike-slip segment with an average strike around 175° and with nearly vertical dip westward direction (SF1 fault); (2) the oriented NNE-SSW strike-slip segment with average strike around 189° with high dip angle (SF2 fault); (3) an oriented E-W normal fault segment (NF fault).

Based on those findings, our preferred interpretation is that the presence of two strike-slip segments with NNW-SSE and NNE-SSW trends might correlate with the regional structure trends in Halmahera, north of the study area (see Fig. 1a). The onshore volcano-chain segment in Halmahera is overlain by a graben-like median zone of an anticline and is bounded to the east by a sequence of steep NNW-SSE trending faults (Verstappen 1964; Passarelli et al. 2018). Hall (1987) also discovered a series of steep faults trending NE-SW and active since the Pliocene with dip-slip and strike-slip motion in Kau Bay. An identical strike-slip mechanism with either NNW-SSE or NEE-WSW is also observed on Buru Island from the CMT solution. Regarding the E-W normal fault segments in Ambon Island, we correlate this with the finding of displacement velocity by Patria et al (2021) in which they showed that the GPS velocity of Ambon and Banda Arc increases toward the east. This region's normal faults are reasonably related to this eastward velocity increase, which causes extensional deformation in the E-W strikes along the Amahai, Ambon, and Buru. In agreement with

our interpretation, Spakman and Hall (2010) hypothesized a Banda Subduction rollback mechanism to explain extensional deformation in a converging zone.

Spatiotemporal seismicity of the aftershock sequences

Figure 12a–d shows the spatiotemporal seismicity of the 2019 Ambon aftershock. We compiled our aftershock data (18 October to 15 December 2019) with the earlier aftershock data (25 to 30 September 2019) from Sianipar et al. (2022), added by aftershock data (1 to 17 October 2019) from Meilano et al. (2021). The focal mechanism solutions for the first 20 days after the mainshock were obtained from Global CMT, while the solution for the next three periods was obtained from the current study. Figure 12a shows the aftershock distribution in the first 20 days after the mainshock. The distribution of aftershocks is mostly dominated by the north–south trend from Kairatu to the south on the Haruku Strait and the low intensity of the event appearance on Ambon Island. Based on the slip inversion results by Sahara et al. (2021a) and the coseismic slip model by Meilano et al. (2021), the mainshock unilaterally ruptured the South and this pattern is possibly making the N-S trends in the early period. The low intensity, as well as the sparse distribution of aftershocks in this period, could not give a clear lineament rupture in Ambon Island. However, during this period, we could observe that there were two significant aftershock events with magnitude $> Mw 5.0$ with two different mechanisms, i.e., normal fault around 3 km east of the N-S trend (labeled as Ag1) and strike-slip fault on Ambon Island (labeled as Ag 2).

In 21–40 days after the mainshock (Fig. 12b), in which 11 temporary local broadband seismometer was included in the monitoring, the aftershock distribution is well-constrained in three rupture areas. In this period, we can observe the first strong lineament of the NNE-SSW of the Ambon cluster (shown by a dashed circle and defined by SF1 fault in Sect. 5.3). There is also an indication of the first appearance of NE-SW aftershock trends in the southwest of Seram (black dashed circle) associated with the reverse fault mechanism.

For the next term, Fig. 12c shows the seismicity in the 41–60 days after the mainshock. The most significant feature that occurred in this term is the extension of rupture propagation in Ambon Island to the northeast direction. The existence of the normal fault cluster in Ambon Island was also observed in this sequence. In more detail, from Fig. 12b, c we could interpret that aftershock sequence in Ambon Island began with a rupture of the NNW-SSE strike-slip (SF1 in Fig. 11b) represented by the focal solution of A2. The rupture continued to the east and northeast just after the occurrence of the largest aftershock with Mw 5.1 on November 12th, 2019 at 10:10:40 (focal

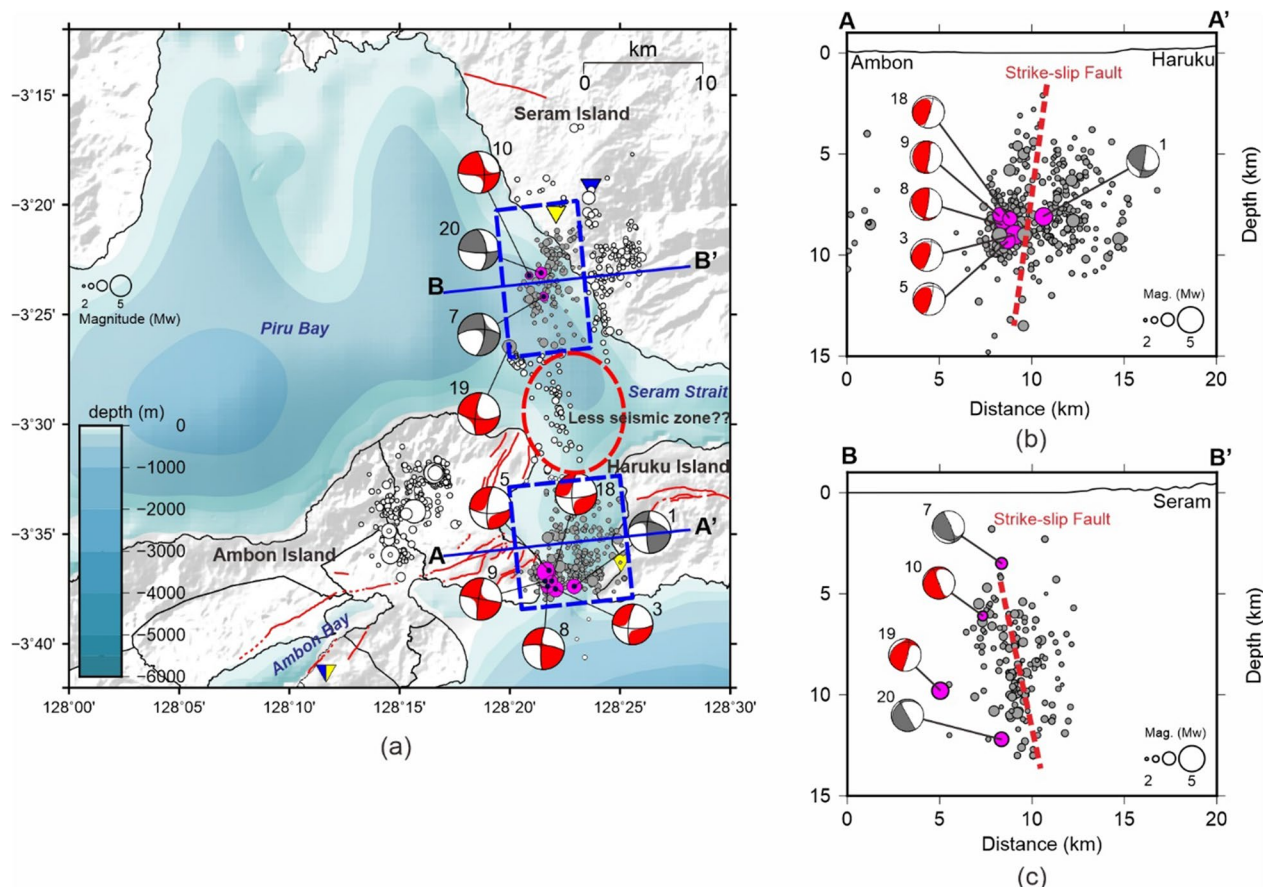


Fig. 9 **a** Map view of focal mechanism distribution along N-S main rupture. The blue dashed rectangles show the area of the beachball and the aftershock hypocenter covered by lines A-A' and B-B' (depicted by blue lines) in a radius of 6 km. The red straight lines show the fault segments mapped by Patria et al. (2021). The red dashed circle depicts the less seismic zone in the central part of region I. **b** Vertical cross-sections of focal mechanism solutions and hypocenter distributions along lines A-A'. **c** Vertical cross-sections of focal mechanism solutions and hypocenter distributions along lines B-B'. Focal mechanisms obtained in this study are plotted as colored beachballs based on Frölich (1992) and Hallo et al. (2017, 2019) with numeric labels to indicate the event ID. The size of the circles represents event magnitudes in Mw. The red dashed lines are the interpreted fault planes derived in this study. The magenta circle plotted in (a–c) is the event hypocenter of the corresponding beach ball solution

solution A11) which was followed by Mw 4.1 at 11:01:44 UTC (focal solution A12). Both event solutions have strike-slip mechanisms with NNE-SSW and NNW-SSE trends (SF2 in Fig. 11b). The E-W normal faults (NF in Fig. 11b) appear simultaneously with the SF2 strike-slip segment, characterized by both Mw 4.9 (focal solution A13) and Mw 4.4 (focal solution A14). In the main N-S cluster, the increase of aftershocks occurred intensively in the south end. Meanwhile, in the north, the seismicity is not so significant but it is still clear enough to describe the event propagation of both strike-slip and reverse fault events in the southwest of Seram. During the last period (61–80 days) after the mainshock (Fig. 12d), low-intensity of seismicity was observed in all three clusters.

Figure 13 below shows the temporal evolution of the aftershock in term of the cumulative number of events in which we associated it with the occurrence of the significant aftershock. We observed the most significant increasing event occurred in the first 5 days after the mainshock and was followed by a gradual decay until the break of the Mw 5.0 (11/10/2019 04:39:43 UTC) in Ambon Island. Besides this Mw 5.0 aftershock, two other significant aftershocks influenced most of the increased seismicity, i.e., Mw 4.7 (18/10/2019 19:44:24 UTC) and Mw 5.1 (12/11/2019 10:10:40 UTC), depicted by the steep increase of the cumulative lines (magenta circles). All these significant aftershocks occurred on Ambon Island.

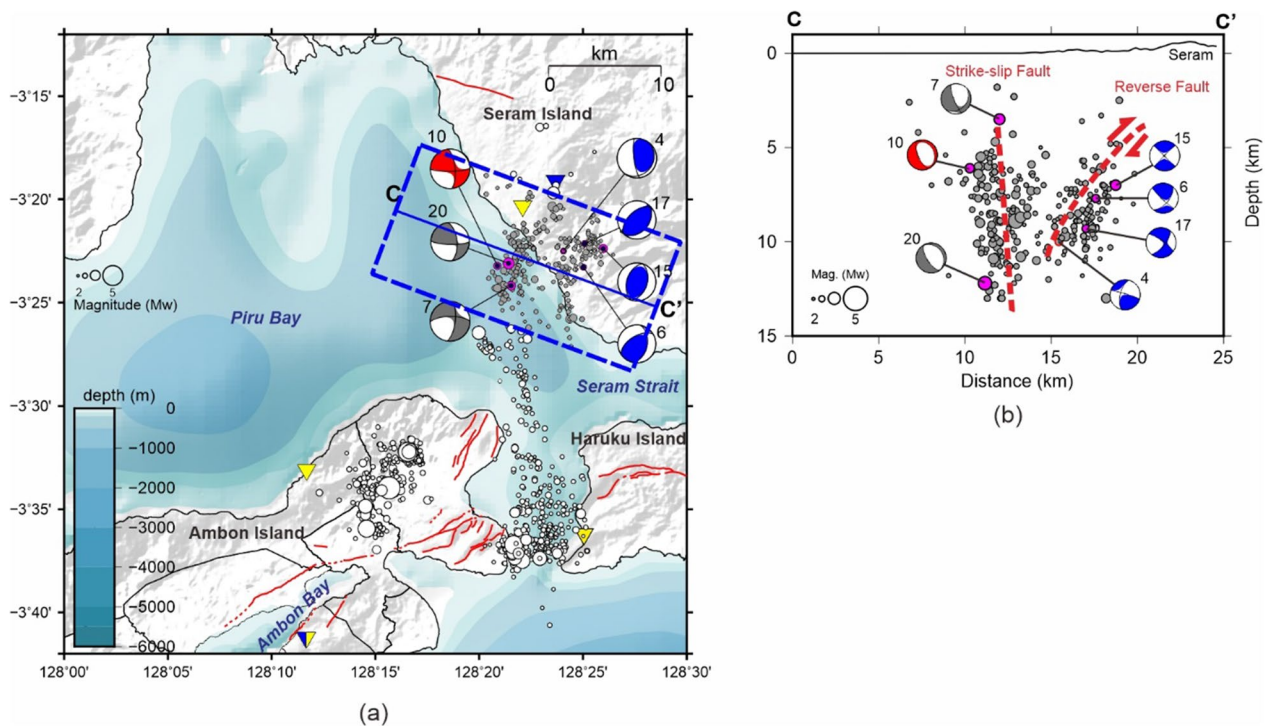


Fig. 10 **a** Map view of focal mechanism distribution in the northern part of the study area. The blue dashed rectangles show the area of the beachball and the aftershock hypocenter covered by lines C–C' (depicted by a blue line) in a radius of 6 km. The red straight lines show the fault segments mapped by Patria et al. (2021). **b** Vertical cross-sections of focal mechanism solutions and hypocenter distributions along lines C–C'. Focal mechanisms obtained in this study are plotted as colored beachballs based on Frohlich (1992) and Hallo et al. (2017, 2019) with numeric labels to indicate the event ID. The size of the circles represents event magnitudes in Mw. The red dashed lines are the interpreted fault planes derived in this study. The magenta circle plotted in (a) and (b) is the event hypocenter of the corresponding beach ball solution

Analysis of the mainshock MTs decomposition and the relation with the aftershock sequence

It is worth addressing how the ruptures occurred during the mainshock and aftershock and their relationship (i.e., joint movement or a series of different fault reactivation). In the 2019 Ambon Earthquake case, we found no indication of joint movements. From our results on the MTs decomposition of the mainshock (see Fig. 8), it might be revealed that the source of the mainshock consists of a major strike-slip and minor normal fault, which indicate that the N-S main fault cluster might observe the presence of a small portion of normal fault aside of strike-slip mechanism. However, all MTs

solutions in this cluster consistently show strike-slip mechanisms which means normal faulting resulting from MTs decomposition is insignificant. This result also shows that the mainshock MTs solution from global CMT (84% of major strike-slip and 16% of minor normal fault in the scalar moment) is more reliable and reasonable compared with the GFZ that reflects the significant percentage of minor normal fault (31.9%).

On the other hand, according to Meilano et al. (2021), the earthquake ruptured two faults that are practically orthogonal to each other: the first fault going roughly north–south, and the second fault trending roughly east–west. This data raise the possibility that the Ambon

(See figure on next page.)

Fig. 11 **a** Seismotectonic information in the south of Northern Banda Arc, by compiling the onshore active faults by Patria et al. (2021) (red lines) and the Global CMT solution (navy beach balls) for inland events with depth < 20 km and a magnitude more than Mw 5 in the period of 1976–2018 **b** Interpretation of fault reactivations in Ambon Island by combining aftershock distribution, source mechanism, and geological fault data by Patria et al. (2021). The aftershock epicenters are plotted with green circles with increased size following the magnitude values. Focal mechanisms obtained in this study are plotted as navy beachballs following the magnitude size with numeric labels to indicate the event ID. The red straight lines show the fault segments mapped by Patria et al. (2021), dominated by dip-slip faults (notated by Up-Down labels: U-D), while the interpreted faults are represented by red dashed lines. **c** Vertical cross-sections of the aftershock earthquake sequence in Ambon Island on line D–D'. The aftershock events are represented by green circles, which its size represents the magnitude value in Mw. Focal mechanisms obtained in this study are plotted as navy beach balls following the magnitude size with numeric labels to indicate the event ID. Label SF1 and SF2 represent two strike-slip faults and NF represents normal faults. The red dashed lines reflect the interpreted strike-slip fault planes

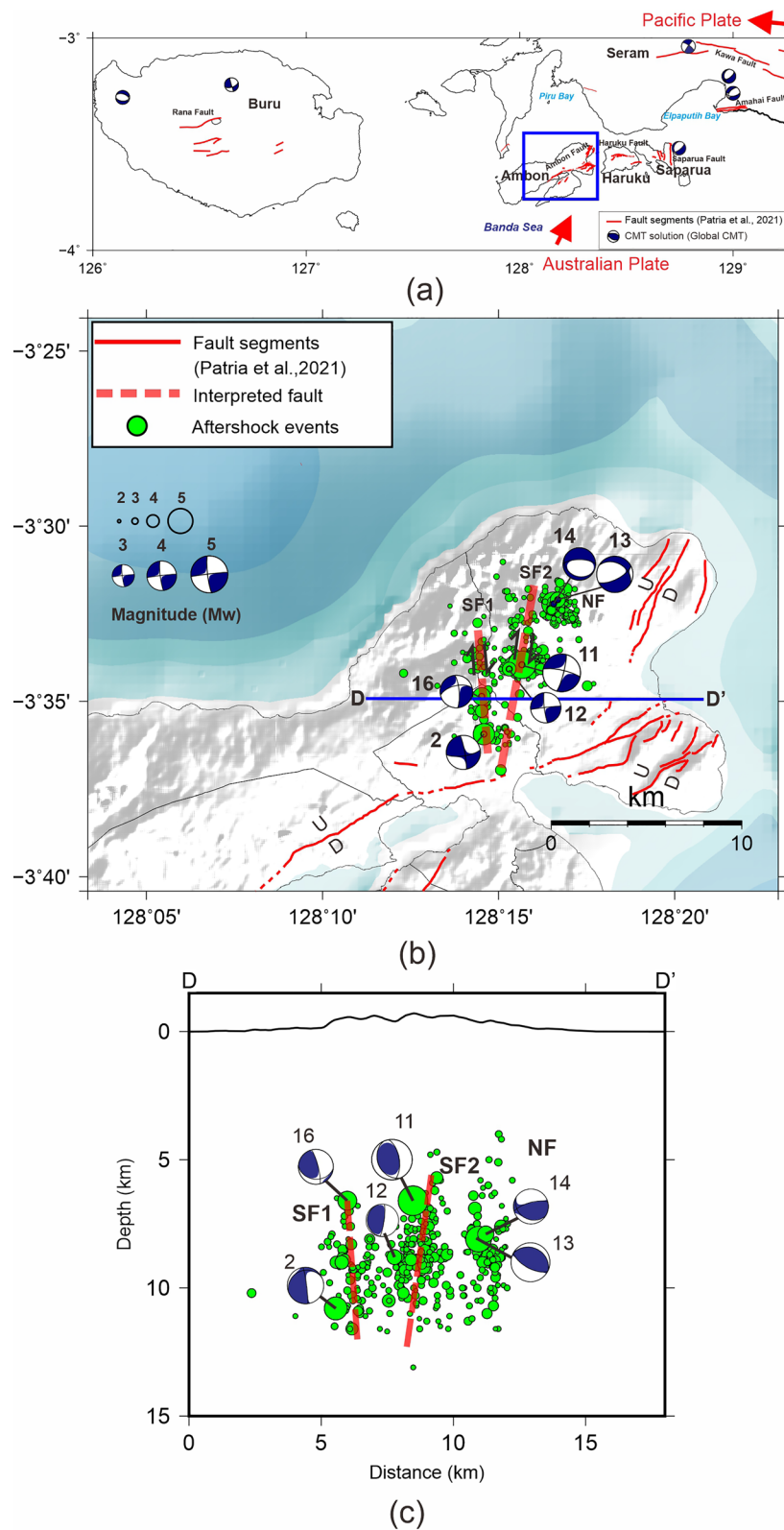


Fig. 11 (See legend on previous page.)

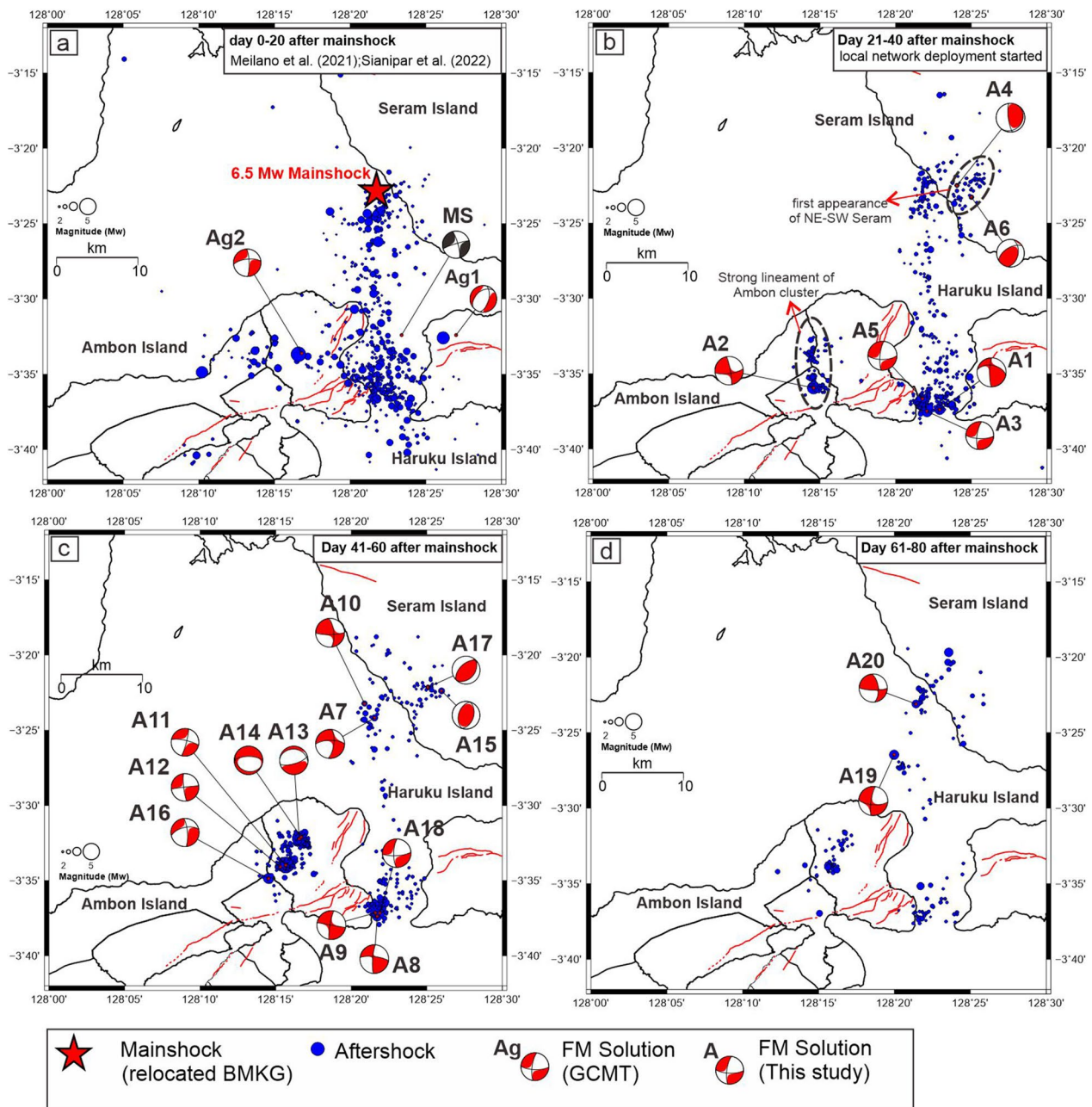


Fig. 12 Spatiotemporal seismicity of the 2019 Ambon aftershock sequences with the focal mechanism solution between 25 September and 15 December 2019 (0–80 days after mainshock): **a** day 0–20 after the mainshock, the mainshock epicenter from BMKG (relocated) is shown by a red star. **b** day 21–40 after the mainshock. **c** day 41–60 after the mainshock. **d** day 61–80 after the mainshock. The blue circles show the hypocenter distribution in the active period and its size represents the magnitude value in Mw. The hypocenter catalog for Fig. 13a is compiled from Meilano et al. (2021) and Sianipar et al. (2022). The focal mechanism solutions for Fig. 13a are derived from Global CMT (labeled as the letter 'Ag'), while Fig. c-d used our MTs solution (labeled as letter 'A' followed by the event ID). The red straight lines show the fault segments mapped by Patria et al. (2021)

earthquake was caused by conjugate faults that were active at the same time during the aftershock. However, in our monitoring (which has better coverage with local temporary networks), the presence of the E-W lineament

was not detected or was not sufficient to be considered as a conjugate fault. We just found a small portion of the E-W lineament in Ambon Island. Our analysis of the MTs mainshock decomposition and the aftershock MTs

Temporal Evolution of the 2019 Ambon Aftershock Sequence

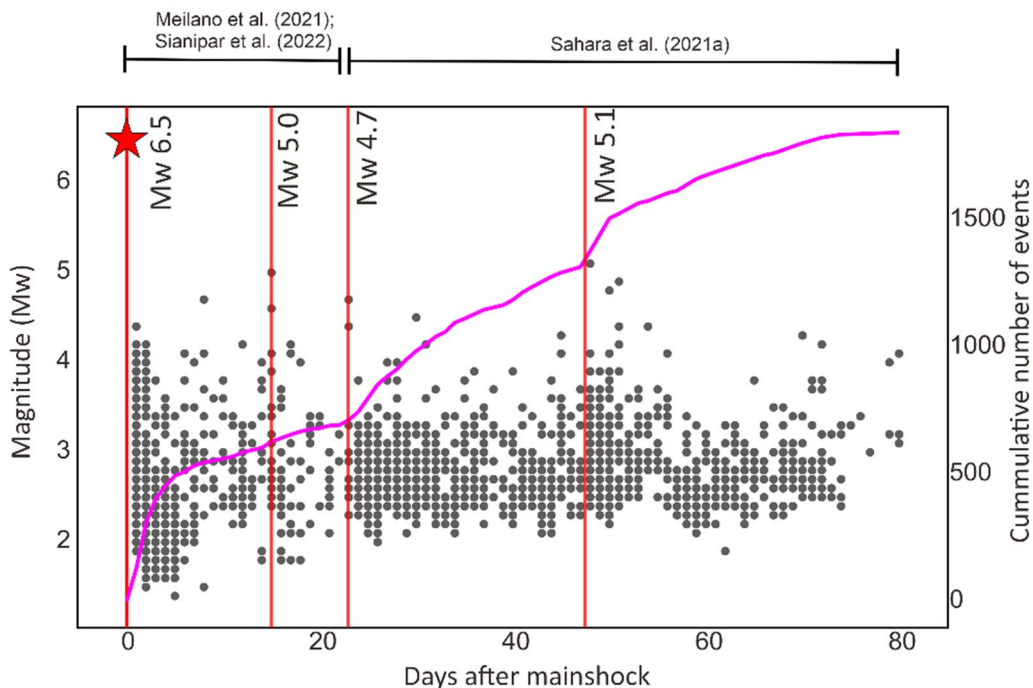


Fig. 13 Temporal evolution of the 2019 Ambon aftershock, visualized by the cumulative number of events within all regions (magenta line) and the occurrence of the daily event ordered based on magnitude (gray circles). The red star shows the mainshock with a magnitude Mw 6.5. The day of the mainshock and several significant aftershock occurrences (which impact the seismicity most) is plotted as red lines

solutions above also confirms that the possibility of the conjugate faults occurring in this 2019 Ambon case is unlikely. Although there are differences in interpretation, both studies consistently revealed the main N-S trends. Therefore, instead of joint movements of different faults, the complexity of the 2019 Ambon aftershock sequence may appear in the form of ruptured locations which clustered in three separated regions, each with its distinctive source mechanism. Thus, we prefer the hypothesis that the Ambon aftershock sequence occurred as a series of separate fault reactivations in a critically stressed area.

Conclusions

The focal mechanism solutions provide a better understanding of fault reactivation in a tropical region where significant surficial processes may erode the trace of active deformation. Using combined local and regional station data, we infer the MT solution for 20 aftershock events of the 2019 Ambon earthquake sequences. This was achieved by carefully selecting the stations used in the inversion, the quality of the waveform, the epicentral distance, and the frequency band utilized for inversion, to satisfy four out of five criteria based on Sokos and Zahradník (2013), including VR, CN, FMVAR, STVAR, and DC parameters.

Our MTs solution could reveal characteristic of fault reactivation in Ambon and Seram region. The N-S main rupture has a 35 km long orientation with the dextral strike-slip mechanism with the dipping changing from westward in the south to eastward in the north separated by a less seismic zone in the middle. Furthermore, we analyzed the fault mechanism of the two reactivated fault clusters from Ambon Island and southwest Seram. The presence of two strike-slip segments with NNW-SSE and NNE-SSW strike orientation in Ambon agree with the regional structure trends in Halmahera, located in the north of the study area, while the E-W oriented normal fault might be related to the eastward velocity increase in Ambon and Banda Arc, which causes extensional deformation. Moreover, the presence of a reverse fault about 5 km east of the N-S main fault in west Seram indicates reactivation of a previously interpreted lineament aligned NE-SW probably due to high-stress transfer imparted by the mainshock.

Analysis of spatiotemporal seismicity with the MTs solution suggests that the Mw 6.5 Ambon mainshock might consist of a geometrically complex rupture. The 2019 Ambon mainshock and its aftershock sequences can be explained as follows: (i) a Mw 6.5 mainshock rupture, characterized by the major strike-slip component

and minor normal fault; (ii) Rupture propagated to the south and making up the first aftershock cluster along the main N-S ruptures, followed by the second cluster in Ambon; (iii) The reverse fault events cluster appeared in the southwest of Seram, in addition with increased seismic activity in the other two clusters.

The triggering of significant fault reactivations due to a relatively moderate Mw 6.5 2019 Ambon earthquake indicates that the faulting regime in the Ambon and Southwest Seram is critically stressed. Moreover, the fault reactivations observed in this study are located nearby the highly populated urban areas of Ambon City and Kairatu. We suggest the stress transfer generated along the fault segments passing through Ambon City in the south of the island should be modeled to estimate the seismic hazard. The reactivation of the small portion of reverse faults in the northern part of the Mw 6.5 main fault indicates that the stability of major NE-SW faults in Seram Island needs to be assessed further. Furthermore, this study provides important insight into active fault identification in Northern Banda Arc.

Abbreviations

MTs	Moment tensors
Mw	Magnitude moment
BMKG	Badan Meteorologi, Klimatologi, dan Geofisika: Agency of Meteorology, Climatology, and Geophysics of Indonesia
BPS	Badan Pusat Statistik: Statistics Indonesia
BNPB	Badan Nasional Penanggulangan Bencana: National Agency for Disaster Management
ISOLA	ISOLated asperities
GCMT	Global centroid moment tensor
GFZ	GeoForschungsZentrum
VR	Variance reduction
CN	Condition number
FMVAR	Focal mechanism variability index
STVAR	Space-time variability index
DC	Double-couple
CLVD	Compensated linear vector dipole
SRTM	Shuttle radar topography mission
CFS	Coulomb failure stress
CFF	Coulomb failure function
SF1	Strike-slip fault 1
SF2	Strike-slip fault 2
NF	Normal fault

Supplementary Information

The online version contains supplementary material available at <https://doi.org/10.1186/s40623-023-01860-1>.

Additional file 1: Figure A1. The correlation between the observed and synthetic waveforms for an aftershock event occurred on October 18th, 2019 with origin time 11:36:23.37. VR values for each station are indicated in blue. The frequency range used for this earthquake is 0.05–0.11 Hz and is shown at the top of the figure. **Figure A2.** The correlation between the observed and synthetic waveforms for an aftershock event occurred on October 18th, 2019 with an origin time of 19:44:24.72. VR values for each station are indicated in blue. The frequency range used for this earthquake is 0.05–0.12 Hz and is shown at the top of the figure. **Figure A3.** The correlation between the observed and synthetic waveforms for an

aftershock event occurred on October 25th, 2019 with origin time 02:08:18.08. VR values for each station are indicated in blue. The frequency range used for this earthquake is 0.05–0.10 Hz and is shown at the top of the figure. **Figure A4.** The correlation between the observed and synthetic waveforms for an aftershock event occurred on October 26th, 2019 with origin time 04:22:44. VR values for each station are indicated in blue. The frequency range used for this earthquake is 0.05–0.11 Hz and is shown at the top of the figure. **Figure A5.** The correlation between the observed and synthetic waveforms for an aftershock event occurred on October 26th, 2019 with an origin time of 19:02:58.44. VR values for each station are indicated in blue. The frequency range used for this earthquake is 0.05–0.11 Hz and is shown at the top of the figure. **Figure A6.** The correlation between the observed and synthetic waveforms for an aftershock event occurred on October 30th, 2019 with origin time 05:04:52.20. VR values for each station are indicated in blue. The frequency range used for this earthquake is 0.04–0.11 Hz and is shown at the top of the figure. **Figure A7.** The correlation between the observed and synthetic waveforms for an aftershock event occurred on November 8th, 2019 with origin time 04:37:07.35. VR values for each station are indicated in blue. The frequency range used for this earthquake is 0.05–0.11 Hz and is shown at the top of the figure. **Figure A8.** The correlation between the observed and synthetic waveforms for an aftershock event occurred on November 9th, 2019 with origin time 03:29:20.49. VR values for each station are indicated in blue. The frequency range used for this earthquake is 0.04–0.10 Hz and is shown at the top of the figure. **Figure A9.** The correlation between the observed and synthetic waveforms for an aftershock event occurred on November 9th, 2019 with an origin time of 15:39:46.86. VR values for each station are indicated in blue. The frequency range used for this earthquake is 0.04–0.11 Hz and is shown at the top of the figure. **Figure A10.** The correlation between the observed and synthetic waveforms for an aftershock event occurred on November 11th, 2019 with origin time 04:35:25.73. VR values for each station are indicated in blue. The frequency range used for this earthquake is 0.05–0.11 Hz and is shown at the top of the figure. **Figure A11.** The correlation between the observed and synthetic waveforms for an aftershock event occurred on November 12th, 2019 with an origin time of 10:40:40.15. VR values for each station are indicated in blue. The frequency range used for this earthquake is 0.04–0.10 Hz and is shown at the top of the figure. **Figure A12.** The correlation between the observed and synthetic waveforms for an aftershock event occurred on November 12th, 2019 with an origin time of 11:01:44.47. VR values for each station are indicated in blue. The frequency range used for this earthquake is 0.05–0.11 Hz and is shown at the top of the figure. **Figure A13.** The correlation between the observed and synthetic waveforms for an aftershock event occurred on November 15th, 2019 with an origin time of 21:02:01.44. VR values for each station are indicated in blue. The frequency range used for this earthquake is 0.04–0.07 Hz and is shown at the top of the figure. **Figure A14.** The correlation between the observed and synthetic waveforms for an aftershock event occurred on November 15th, 2019 with an origin time of 22:30:11.76. VR values for each station are indicated in blue. The frequency range used for this earthquake is 0.04–0.09 Hz and is shown at the top of the figure. **Figure A15.** The correlation between the observed and synthetic waveforms for an aftershock event occurred on November 17th, 2019 with origin time 05:11:21.99. VR values for each station are indicated in blue. The frequency range used for this earthquake is 0.05–0.11 Hz and is shown at the top of the figure. **Figure A16.** The correlation between the observed and synthetic waveforms for an aftershock event occurred on November 18th, 2019 with origin time 09:04:29.90. VR values for each station are indicated in blue. The frequency range used for this earthquake is 0.04–0.08 Hz and is shown at the top of the figure. **Figure A17.** The correlation between the observed and synthetic waveforms for an aftershock event occurred on November 18th, 2019 with an origin time of 13:11:19.47. VR values for each station are indicated in blue. The frequency range used for this earthquake is 0.05–0.11 Hz and is shown at the top of the figure. **Figure A18.** The correlation between the observed and synthetic waveforms for an aftershock event occurred on November 20th, 2019 with an origin time of 21:43:27.90. VR values for each station are indicated in blue. The frequency range used for this earthquake is 0.05–0.11 Hz and is shown at the top of the figure. **Figure A19.** The correlation between the observed and

synthetic waveforms for an aftershock event occurred on December 4th, 2019 with an origin time of 13:48:07.42. VR values for each station are indicated in blue. The frequency range used for this earthquake is 0.04–0.11 Hz and is shown at the top of the figure. **Figure A20.** The correlation between the observed and synthetic waveforms for an aftershock event occurred on December 14th, 2019 with an origin time of 19:43:11.28. VR values for each station are indicated in blue. The frequency range used for this earthquake is 0.04–0.11 Hz and is shown at the top of the figure. **Figure A21.** The correlation between the observed and synthetic waveforms using four different velocity models: crustal model for the central part of Java; PREM; a crustal model for eastern Indonesia, and a new regional crustal model around Ambon derived from Sahara et al. for an aftershock event on November 12th, 2019 with an origin time of 10:40:40.15. VR values for each station are indicated in blue. The frequency range used for this earthquake is 0.04–0.10 Hz. The red cross sign shows the station components with a relatively poor fitting. **Figure A22.** Illustration of FMVAR parameter constructed by all acceptable solutions from MT inversion for event ID 13. The best fit of nodal is shown by red nodal lines. The illustration of STVAR reflects the size of the space-time region corresponding to the given correlation threshold for event ID 13 denoted by black dots. **Figure A23.** The singular vectors V and singular values w_i determine the shape and orientation of the error ellipsoid. The singular vectors V define the orientation of the ellipsoid in 6D-parameter space by determining the direction of the ellipsoid axis. The singular values define the size of the ellipsoid axis, and consequently the ellipsoid's shape. The data error, d , scales the overall size of the ellipsoid. The surface of the ellipsoid is characterized by the $\Delta\chi^2 = \text{constant}$. **Figure A24.** Correlation diagram of focal MTs solution on each trial source depth. The MT solution from the depth of 20 km is used as *mref*. **Figure A25.** the diagram of strike, dip, and rake angles for the family of acceptable solutions versus misfit, $\Delta\chi^2$, for the MT solution reference with a depth of 20 km; strike, dip, rake angles are 300°, 38°, -40°, equivalent to 64°, 67°, -121°. Histograms of the strike, dip, rake, and the nodals. The optimal solution is shown by a red thick line, whereas the dotted-line vertical strips mark the histogram width, interactively determined by the user. **Figure A26.** the diagram of rake angles for the family of acceptable solutions versus misfit, $\Delta\chi^2$ from event ID 9. Histograms of the converted rake angles. The optimal solution is shown by a red thick line, whereas the black dotted-line vertical strips mark the histogram width, interactively determined by the user. For rake 1, the data only distributed on one side, so we could only consider the single range on the right side of the optimal solution. Meanwhile the data from rake 2 show non normal distribution, in which data in the right side contribute more acceptable rakes. In this case, we simply choose the maximum deviation respect to the optimal solution. **Table A1.** Uncertainty of nodal planes from all 20 aftershock events

Acknowledgements

BMKG provided access to their 2019 Ambon aftershocks data recorded by regional seismic networks, which we also utilized in this study. GMT (Wessel et al. 2013), ISOLA MATLAB GUI, Matplotlib's Python, and Plotly's Python were used to create all the figures. BNPB financed the installation of local seismographic networks. The Master Program of AWB (first author) is fully funded by the Lembaga Pengelola Dana Pendidikan (LPDP) organized by the Indonesian Ministry of Finance. We thank Prof. Robert Hall (Royal Holloway, University of London) for reviewing an early version of the manuscript. We also thank Dr. Mochamad Nukman (Geophysics Study Program, Gadjah Mada University, Yogyakarta) for giving his insight into the geological interpretation for the discussion section.

Author contributions

Conceptualization and analysis were performed by AWB, DPS, and ADN. Method and software were provided by AWB. Data collection and resources were provided by ZZ and AAR. The first draft of the manuscript was written by AWB. Supervision was performed by DPS, ADN, SW, and HAS. WT, NTP, AP, DK, AR, and EE commented the initial versions of the manuscript. All authors read and approved the final manuscript.

Funding

This research was funded by Institut Teknologi Bandung KK-A 2022 research fund: "Sulawesi in-situ regional stress map preparation from new focal mechanism dataset as an effort to mitigate geological disasters in Eastern Indonesia" with grant number 829/IT1.C05/KU.02/2022; and by the Program Penelitian Kolaborasi Indonesia (PPKI) Non-APBN Institut Teknologi Bandung with grant number 210/IT1.B07.1/SPP-LPPM/V/2022.

Availability of data and materials

The Ambon aftershock catalog data underlying this article are available in the Mendeley data, v1 repository, at <https://data.mendeley.com/datasets/z5nmbmmdt/1> (Sahara et al. 2021b). The focal mechanism data for the first 20 days after the mainshock were obtained from the Global Centroid Moment Tensor (Global CMT) catalog (Ekström et al. 2012) <https://www.globalcmt.org/CMTsearch.html>. The focal mechanism of the mainshock for the MT decomposition was taken from Global CMT (Ekström et al. 2012) <https://www.globalcmt.org/CMTsearch.html> and GFZ (Saul et al. 2011) <https://geofon.gfz-potsdam.de/old/eqinfo/list.php?mode=mt>. The MTs solution in this current study is directly presented in this paper manuscript (Table 2) and available to use by the reader. The waveform data underlying this article are available upon request to the authors.

Declarations

Ethic approval and consent to participate

Not applicable.

Consent for publication

Not applicable.

Competing interests

The authors declare that they have no competing interests.

Author details

¹Geophysical Engineering Study Program, Institut Teknologi Bandung, Bandung, Indonesia. ²Global Geophysics Research Group, Institut Teknologi Bandung, Bandung, Indonesia. ³Agency of Meteorology, Climatology, and Geophysics of Indonesia, Jakarta, Indonesia. ⁴Faculty of Engineering, Maranatha Christian University, Bandung, Indonesia. ⁵Department of Earth Science, University of Bergen, All'egaten 41, 5007 Bergen, Norway. ⁶Geological Engineering Study Program, Institut Teknologi Bandung, Bandung, Indonesia. ⁷Geological Engineering Study Program, Pattimura University, Ambon, Indonesia.

Received: 6 January 2023 Accepted: 10 June 2023

Published online: 18 August 2023

References

- Abdel-aal AK, Yagi Y (2017) Earthquake source characterization, moment tensor solutions, and stress field of small-moderate earthquakes occurred in the northern Red Sea Triple Junction. *Geosci J* 21:235–251. <https://doi.org/10.1007/s12303-016-0025-x>
- Asano K, Iwata T (2016) Source rupture processes of the foreshock and mainshock in the 2016 Kumamoto earthquake sequence estimated from the kinematic waveform inversion of strong motion data. *Earth, Planets Sp* 68:147. <https://doi.org/10.1186/s40623-016-0519-9>
- Ataei N, Rezapour M (2016) Moment tensor and stress inversion for an active fault system in west part of Lut-block, Iran. *J Earth Sp Phys* 41:13–22. <https://doi.org/10.2205/jesphys.2015.57223>
- Audley-Charles M, Carter D, Barber A, Norvick M, Tjokrosapoetro S (1979) Reinterpretation of the geology of seram: implications for the Banda Arcs and Northern Australia. *J Geol Soc London* 136:547–566
- Baillie P, Keep M, Duran PM, Carrillo E, Duval G (2020) Broadband seismic imaging around the Banda Arc: changes in the anatomy of offshore fold-and-thrust belts. *Fold Thrust Belts Struct Style Evol Explor* 490(1):351–360
- Båth M, Duda SJ (1979) Some aspects of global seismicity. *Tectonophysics* 54:T1–T8. [https://doi.org/10.1016/0040-1951\(79\)90105-7](https://doi.org/10.1016/0040-1951(79)90105-7)

- BNPB (2019) Data/Informasi Kejadian Bencana Dan Dampak Bencana Gempa Ambon 2019 (Field survey report). <https://doi.org/10.17632/tbnhg37jxx.1>
- Bock Y (2003) Crustal motion in Indonesia from global positioning system measurements. *J Geophys Res*. <https://doi.org/10.1029/2001jb000324>
- Bock Y, Prawirodirdjo L, Genrich JF, Stevens CW, McCaffrey R, Subarya C, Puntodewo SSO, Calais E (2003) Crustal motion in Indonesia from global positioning system measurements. *J Geophys Res Solid Earth*. <https://doi.org/10.1029/2001JB000324>
- Bouchon M (1981) A simple method to calculate Green's functions for elastic layered media. *Bull Seismol Soc Am* 71:959–971
- BPS (2021) Potret Sensus Penduduk 2020 Provinsi Maluku
- Brune S, Babeyko AY, Ladage S, Sobolev SV (2010) Landslide tsunami hazard in the Indonesian sunda arc. *Nat Hazards Earth Syst Sci* 10:589–604. <https://doi.org/10.5194/nhess-10-589-2010>
- Cesca S, Buforn E, Dahm T (2006) Amplitude spectra moment tensor inversion of shallow earthquakes in Spain. *Geophys J Int* 166:839–854. <https://doi.org/10.1111/j.1365-246X.2006.03073.x>
- DeMets C, Gordon RG, Argus DF (2010) Geologically current plate motions. *Geophys J Int* 181:1–80. <https://doi.org/10.1111/j.1365-246X.2009.04491.x>
- Dziewonski AM, Anderson DL (1981) Preliminary reference earth model. *Phys Earth Planet Inter* 25:297–356. [https://doi.org/10.1016/0031-9201\(81\)90046-7](https://doi.org/10.1016/0031-9201(81)90046-7)
- Eksström G, Nettles M, Dziewoński AM (2012) The global CMT project 2004–2010: centroid-moment tensors for 13,017 earthquakes. *Phys Earth Planet Inter* 200:1–9. <https://doi.org/10.1016/j.pepi.2012.04.002>
- Engdahl ER, van der Hilst R, Buland R (1998) Global teleseismic earthquake relocation with improved travel times and procedures for depth determination. *Bull Seismol Soc Am* 88:722–743
- Frohlich C (1992) Triangle diagrams: ternary graphs to display similarity and diversity of earthquake focal mechanisms. *Phys Earth Planet Inter* 75:193–198. [https://doi.org/10.1016/0031-9201\(92\)90130-N](https://doi.org/10.1016/0031-9201(92)90130-N)
- Fukahata Y, Hashimoto M (2016) Simultaneous estimation of the dip angles and slip distribution on the faults of the 2016 Kumamoto earthquake through a weak nonlinear inversion of InSAR data. *Earth Planets Sp* 68:204. <https://doi.org/10.1186/s40623-016-0580-4>
- Hall R (1987) Plate boundary evolution in the Halmahera region, Indonesia. *Tectonophysics* 144:337–352. [https://doi.org/10.1016/0040-1951\(87\)90301-5](https://doi.org/10.1016/0040-1951(87)90301-5)
- Hall R, Patria A, Adhitama R, Pownall JM, White L (2017) Seram, the seram trough, the aru trough, the tanimbar trough and the weber deep: a new look at major structures in the eastern banda arc. Indonesian Petroleum Association, Jakarta
- Hallo M, Asano K, Gallovič F (2017) Bayesian inference and interpretation of centroid moment tensors of the 2016 Kumamoto earthquake sequence, Kyushu, Japan 4. seismology. *Earth, Planets Sp* 69:1–19. <https://doi.org/10.1186/s40623-017-0721-4>
- Hallo M, Opršal I, Asano K, Gallovič F (2019) Seismotectonics of the 2018 northern Osaka M6.1 earthquake and its aftershocks: joint movements on strike-slip and reverse faults in inland Japan. *Earth Planets Sp*. <https://doi.org/10.1186/s40623-019-1016-8>
- Harris R, Major J (2016) Waves of destruction in the East Indies: the wickmann catalogue of earthquakes and tsunami in the Indonesian region from 1538 to 1877. *Geol Soc*. <https://doi.org/10.1144/SP441.2>
- Herman M, Nealy J, Yeck W, Barnhart W, Hayes G, Furlong K, Benz H (2017) Integrated geophysical characteristics of the 2015 Illapel, Chile, Earthquake: the illapel earthquake sequence. *J Geophys Res Solid Earth*. <https://doi.org/10.1002/2016JB013617>
- Jost ML, Herrmann RB (1989) A student's guide to and review of moment tensors. *Seismol Res Lett* 60:37–57. <https://doi.org/10.1785/gssrl.60.2.37>
- Kanamori H, Given JW (1982) Use of long-period surface waves for rapid determination of earthquake source parameters 2. Preliminary determination of source mechanisms of large earthquakes ($M_S \geq 6.5$) in 1980. *Phys Earth Planet Inter* 30:260–268. [https://doi.org/10.1016/0031-9201\(82\)90112-1](https://doi.org/10.1016/0031-9201(82)90112-1)
- Kissling E, Kradolfer U, Maurer H (1995) VELEST user's guide—short introduction Koulakov I, Bohm M, Asch G, Lühr BG, Manzanares A, Brotopuspito KS, Fauzi P, Purbawinata MA, Puspito NT, Ratdomopurbo A, Kopp H, Rabbel W, Shevkunova E (2007) P and S velocity structure of the crust and the upper mantle beneath central Java from local tomography inversion. *J Geophys Res Solid Earth*. <https://doi.org/10.1029/2006JB004712>
- Løvholt F, Kühn D, Bungum H, Harbitz CB, Glimsdal S (2012) Historical tsunamis and present tsunami hazard in eastern Indonesia and the southern philippines. *J Geophys Res Solid Earth*. <https://doi.org/10.1029/2012JB009425>
- Lozos J (2021) The effect of along-strike variation in dip on rupture propagation on strike-slip faults. *Geosphere*. <https://doi.org/10.1130/GE502.391.1>
- McCaffrey R (1989) Seismological constraints and speculations on Banda arc tectonics. *Netherlands J Sea Res* 24:141–152
- Meilano I, Salman R, Rahmadani S, Shi Q, Susilo S, Lindsey E, Supendi P, Daryono D (2021) Source characteristics of the 2019 mw 6.5 Ambon, Eastern Indonesia, Earthquake inferred from seismic and geodetic data. *Seismol Res Lett* 92:3339–3348. <https://doi.org/10.1785/0220210021>
- Passarelli L, Heryandoko N, Cesca S, Rivalta E, Rasmid RS, Dahm T, Milkereit C (2018) Magmatic or not magmatic? The 2015–2016 seismic swarm at the long-dormant Jailolo Volcano, West Halmahera Indonesia. *Front Earth Sci* 6:79. <https://doi.org/10.3389/feart.2018.00079>
- Patria A, Hall R (2017) The origin and significance of the Seram trough, Indonesia: Indonesian petroleum association. Forty-First Annual Convention & Exhibition, Jakarta
- Patria A, Tsutsumi H, Natawidjaja DH (2021) Active fault mapping in the onshore northern Banda Arc, Indonesia: implications for active tectonics and seismic potential. *J Asian Earth Sci* 218:104881. <https://doi.org/10.1016/j.jseas.2021.104881>
- Paul H, Priestley K, Powal D, Sharma S, Mitra S, Wanchoo S (2018) Signatures of the existence of frontal and lateral ramp structures near the kishwar window of the Jammu and Kashmir Himalaya: evidence from microseismicity and source mechanisms. *Gechem Geophys Geosyst* 19:3097–3114. <https://doi.org/10.1029/2018GC007597>
- Petersen G, Cesca S, Heimann S, Niemi P, Dahm T, Kühn D, Kummerow J, Pleinefisch T (2021) Regional centroid moment tensor inversion of small to moderate earthquakes in the Alps using the dense AlpArray seismic network: challenges and seismotectonic insights. *Solid Earth* 12:1233–1257. <https://doi.org/10.5194/se-12-1233-2021>
- Pownall JM, Hall R, Watkinson IM (2013) Extreme extension across Seram and Ambon, eastern Indonesia: evidence for Banda slab rollback. *Solid Earth* 4:277–314. <https://doi.org/10.5194/se-4-277-2013>
- Sabtaji A, Nugraha AD (2015) 1-D seismic velocity model and hypocenter relocation using double difference method around West Papua region. *AIP Conf Proc*. <https://doi.org/10.1063/14915013>
- Sahara David P, Nugraha AD, Muhari A, Rusdin AA, Rosalia S, Priyono A, Zulfakriza Z, Widiyantoro S, Puspito NT, Rietbrock A, Lesmana A, Kusumawati D, Ardianto A, Baskara AW, Halauwet Y, Shiddiqi HA, Rafie MT, Pradisti R, Mozef PW, Tuakia MZ, Elly E (2021a) Source mechanism and triggered large aftershocks of the Mw 6.5 Ambon Indonesia earthquake. *Tectonophysics* 799:228709. <https://doi.org/10.1016/j.tecto.2020.228709>
- Sahara David P, Nugraha AD, Muhari A, Rusdin AA, Rosalia S, Priyono A, Zulfakriza Z, Widiyantoro S, Puspito NT, Lesmana A, Kusumawati D, Ardianto A, Baskara AW, Halauwet Y, Shiddiqi HA (2021b) 2019 Ambon aftershocks catalogue data compiled using local and regional seismic networks. *Data Br* 34:106728. <https://doi.org/10.1016/j.dib.2021.106728>
- Saul J, Becker J, Hanka W (2011) Global moment tensor computation at GFZ Potsdam. AGU Fall Meet, San Francisco, USA, abstract ID. S51A-2202
- Serpetsidaki A, Sokos E, Tselentis GA, Zahradnik J (2010) Seismic sequence near Zakynthos Island, Greece, April 2006: Identification of the activated fault plane. *Tectonophysics* 480:23–32. <https://doi.org/10.1016/j.tecto.2009.09.024>
- Sianipar D, Daryono D, Halauwet Y, Ulfiana E, Sipayung R, Daniarsyad G, Heryandoko N, Prasetyo RA, Serhalawan Y, Karnawati D (2022) Intense foreshock swarm preceding the 2019 MW 6.5 Ambon (Seram, Indonesia) earthquake and its implication for the earthquake nucleation process. *Phys Earth Planet Inter* 322:106828. <https://doi.org/10.1016/j.pepi.2021.106828>
- Sokos EN, Zahradnik J (2008) ISOLA a Fortran code and a Matlab GUI to perform multiple-point source inversion of seismic data. *Comput Geosci* 34:967–977. <https://doi.org/10.1016/j.jageo.2007.07.005>
- Sokos E, Zahradnik J (2013) Evaluating centroid-moment-tensor uncertainty in the new version of ISOLA software. *Seismol Res Lett* 84:656–665. <https://doi.org/10.1785/0220130002>

- Spakman W, Hall R (2010) Surface deformation and slab–mantle interaction during Banda arc subduction rollback. *Nat Geosci* 3:562–566. <https://doi.org/10.1038/ngeo917>
- Stevens CW, McCaffrey R, Bock Y, Genrich JF, Pubellier M, Subarya C (2002) Evidence for block rotations and basal shear in the world's fastest slipping continental shear zone in NW New Guinea. In: Stein S, Freymueller JT (eds) Plate boundary zones (Geodynamic). Am Geophys Union, Washington
- Teas P (2009) New insight into structure and tectonics of the seram trough from SeaSeap™ high resolution bathymetry Indonesian petroleum association. Thirty-Third Annual Convention & Exhibition, Jakarta
- Umino N, Okada T, Nakajima J, Hori S, Kono T, Nakayama T, Uchida N, Shimizu J, Suganomata J, Gamage SSN, Hasegawa A, Asano Y (2003) Hypocenter and focal mechanism distributions of aftershocks of July 26 2003 M6.4 northern Miyagi, NE Japan, earthquake revealed by temporary seismic observation. *Earth Planets Sp* 55:719–730. <https://doi.org/10.1186/BF03352481>
- Verstappen HT (1964) Some volcanoes of halmahera (moluccas) and their geomorphological setting. *K Ned Aardrijkskd Genoot* 81:297–316
- Wallace TC (1985) A reexamination of the moment tensor solutions of the 1980 Mammoth Lakes Earthquakes. *J Geophys Res Solid Earth* 90:11171–11176. <https://doi.org/10.1029/JB090iB13p11171>
- Watkinson IM, Hall R (2017) Fault systems of the eastern Indonesian triple junction: evaluation of quaternary activity and implications for seismic hazards. *Geol Soc Spec Publ* 441:71–120. <https://doi.org/10.1144/SP441.8>
- Wessel P, Smith WHF, Scharroo R, Luis J, Wobbe F (2013) Generic mapping tools: improved version released. *Eos Trans Am Geophys Union* 94:409–410. <https://doi.org/10.1002/2013EO450001>
- Zahradnik J, Custódio S (2012) Moment tensor resolvability: application to Southwest Iberia. *Bull Seismol Soc Am* 102:1235–1254. <https://doi.org/10.1785/0120110216>
- Zheng Y, Ni S, Xie Z, Lv J, Ma H, Sommerville P (2010) Strong aftershocks in the northern segment of the Wenchuan earthquake rupture zone and their seismotectonic implications. *Earth Planets Sp* 62:881–886. <https://doi.org/10.5047/eps.2009.06.001>

Publisher's Note

Springer Nature remains neutral with regard to jurisdictional claims in published maps and institutional affiliations.

Submit your manuscript to a SpringerOpen® journal and benefit from:

- Convenient online submission
- Rigorous peer review
- Open access: articles freely available online
- High visibility within the field
- Retaining the copyright to your article

Submit your next manuscript at ► [springeropen.com](https://www.springeropen.com)
